Performance Optimization of Lifetime Sensitive Devices Based on Coupled Optical, Process, and Device Modeling

Armin Yazdani

A dissertation

submitted in partial fulfillment of the

requirements for the degree of

Doctor of Philosophy

University of Washington

2015

Reading Committee:

Scott T. Dunham, Chair

Manjeri Anantram

Lih-Yuan Lin

Program Authorized to Offer Degree:

Electrical Engineering

University of Washington

Abstract

Performance Optimization of Lifetime Sensitive Devices Based on Coupled Optical, Process, and Device Modeling

Armin Yazdani

Chair of the Supervisory Committee:
Professor Scott T. Dunham
Electrical Engineering

The market for silicon electronic devices such as photovoltaics and image sensors has been experiencing explosive growth in recent years. Silicon solar cells are gathering increasing attention as promising means of satisfying part of the growing need for green energy supply and recent advances in the design of complementary-metal-oxide-semiconductor (CMOS) image sensors have led to their adoption in several high volume products incorporating mobile imaging and digital still and video cameras. Such devices are sensitive to carrier lifetime and their fabrication requires precise control of impurities and defects present in the silicon wafers. Failure to do so not only degrades the performance and efficiency, it also poses a great threat to the survival of commercial electronics companies in today's competitive market.

Particularly, in order to enable solar cells to significantly contribute to the world's energy resources further cost reduction must be accomplished by enhancing their efficiencies through development of new technologies and optimization of their device structures and processes. Complex modern processes involving multiple thermal steps make this impossible without the aid of computational models which help us gain better understanding of the involved atomic processes and their impact on the device performance. In this dissertation a reliable and comprehensive TCAD framework is developed establishing the connection between processing conditions and the resulting device performance. It also provides us with optimization tools in a cost-effective way simply because the cost of experiments are increasing as process equipment becomes more expensive and complex.

The focus of this dissertation, in the process modeling, was on the gettering of transition metals. The competitive gettering of metal impurities (Cu, Ni, Fe, Mo, and W) by boron doped, phosphorus doped regions, and dislocation loops was modeled. *Ab initio* density functional theory calculations were first performed to determine the binding energies of metals to the gettering sites, and based on that, continuum models were developed to model the redistribution and trapping of the metals. Critical model parameters were calibrated against experimental measurements. It was found that Fe is most strongly trapped by the dislocation loops while Cu and Ni are most strongly trapped by the P4V clusters formed in high phosphorus concentrations. In addition, it is found that none of the mentioned gettering sites are effective in trapping Mo and W. Finally, the calculated metal redistribution was coupled with device simulation via Shockley-Read-Hall recombination model to calculate carrier lifetime and the resulting device performance. Thereby, processing conditions and performance of a generic image sensing photodiode was optimized. The TCAD framework can be extended to other ULSI devices, as well.

Also, the performance of a textured metal-wrap-through solar cell were analyzed using coupled optical and device 3D numerical simulations. All of the models and parameters in the simulation were calibrated based on experimental measurements. The simulation results were very close to the measurements done on fabricated devices, demonstrating the reliability of the developed TCAD framework for solar cell optimization. The opportunities to attain efficiencies exceeding 20% were investigated.

TABLE OF CONTENTS

LIST OF FIGURES

LIST OF TABLES

ACKNOWLEDGEMENTS

My deepest gratitude goes to my advisor, Professor Scott T. Dunham, for being a great mentor to me and supporting my research for more than 5 years. His guidance and impressive knowledge has made my Ph.D. period such an enriching and formative experience.

I would like to thank Professors Anant Anantram, Lih Y. Lin, and Jim Pfaendtner who accepted to serve as my reading committee. I have also had a great experience of taking the Quantum Mechanics for Engineers course with Professor Anantram who was a pleasure to interact with and learn from.

Funding for my research was generously provided by Solar World Inc. and Sony Corporation. I would especially like to thank Mr. Guenther Mueller, and Mr. Satoshi Yamanaka from Solar World Inc. for their collaborative efforts. All the experimental measurements for MWT solar cells were conducted by them at Solar World Inc.

I would also like to express my love and gratitude to my family for all the sacrifices, love, encouragements and support I have received from them. They were with me every step of the way, sharing the triumphs and anxieties. Thank you Shahpar, Hossein and Negin!

DEDICATION

To my beloved parents, Shahpar and Hossein, for their unconditional love, support, guidance, and all their sacrifices.

And to my teachers, who extended my world, for inspiration they gave me.

Chapter 1. INTRODUCTION

As integrated circuit processes and devices become more complex and advanced, solving analytical equations associated with device physics and processing becomes more difficult. Devices with finer dimensions and shallower junction depths require second-order physical effects to be considered in their design and analysis. Also, various physical mechanisms involved need to be studied in the atomic scale and complex interactions between critical elements of the system such as dopants, defects, impurities, and external influences have to be considered in the analysis and design of Ultra-Large-Scale-Integration (ULSI) devices. Conducting meaningful experiments is also becoming difficult at the same time. The experimental control needed to clearly reveal the effects being studied can exceed the limits and the cost of experiments is increasing as process equipment becomes more expensive and complex involving a large number of thermal processing steps. In addition, the decreasing flexibility of automated equipment in the ULSI technology makes experiments more difficult to be performed. Moreover, the overwhelming number of possible variations in the device structure and processing conditions make studying all variables experimentally impossible.

In contrast, numerical simulations become increasingly attractive as detailed physical models for devices and processes are continually being improved and more accurate and readily available computers become more powerful. With the aid of numerical simulations we can gain better understanding of the physical mechanisms involved, and thereby design more efficient fabrication process steps and device architectures. Beside ULSI devices, silicon solar cells can also increasingly benefit from numerical simulations. Improvement in efficiency are slow and

incremental and even a modest improvement in the yield by better fabrication strategies and architectural designs is lucrative.

The objective of this dissertation is to develop a comprehensive and accurate technology computer aided design (TCAD) framework capable of predicting the device performance based on the impurity content, the processing conditions, and the resulting device structures. The focus of this dissertation is on lifetime sensitive silicon optoelectronic devices such as silicon solar cells and image sensors, however the framework and approach is extendable to other ULSI devices, as well. The modeling approach is based on coupling between detailed process, optical, and device numerical calculations, thereby the influence of various fabrication processes and possible device architectures on their performance can be studied and optimized in a cost-effective way.

1.1 Device Simulations

Device modeling provides information about behavior of electrons and holes throughout the device and from that calculates the overall electrical characteristics of electronic devices. Models are based on solution of Poisson's equation [5] and the continuity equations [5]. Poisson's equation describes the electrostatic potential in terms of the fixed and mobile charges in the device:

$$\nabla^2\phi = -\frac{\rho}{\epsilon} = -\frac{q}{\epsilon}(p - n + N_d^+ - N_a^-) - \frac{\rho_f}{\epsilon} \tag{1.1}$$

where ρ represents the space-charge density, N_d^+ and N_a^-represent the ionized donors and acceptors, q represents the electron charge, ρ_f represents the fixed charge density (useful when interfaces with insulators are being considered), ϵ is the silicon permittivity, p represents the hole density, and n represents the electron density. The continuity equations describe the carrier concentrations:

$$\frac{\partial n}{\partial t} = \frac{1}{q}\nabla . J_n + (G - R) \tag{1.2}$$

$$\frac{\partial p}{\partial t} = -\frac{1}{q}\nabla . J_p + (G - R) \tag{1.3}$$

where J_n and J_p represents electron and hole current densities respectively, G represent the rate at which electron-hole pairs are generated, and R represent the rate at which electrons and holes are recombined. Carriers' migration in the lattice is due to drift and diffusion and is modeled by:

$$J_n = q\mu_n n\mathcal{E} + qD_n \frac{\partial n}{\partial x} \tag{1.4}$$

$$J_p = q\mu_p p\mathcal{E} - qD_p \frac{\partial p}{\partial x} \tag{1.5}$$

where μ_n and μ_p are electron and hole mobility in the silicon lattice respectively, D_n and D_p are electron and hole diffusivities (or diffusion coefficients) in the silicon lattice respectively, and $\mathcal{E}$ is the electrical field which is calculated by the Poisson's equation. The relationship between carriers' diffusion coefficient and mobility is governed by the Einstein relation:

$$D = \frac{kT}{q}\mu \tag{1.6}$$

In which, k is the Boltzmann's constant and T is the absolute temperature.

The initial and boundary conditions to these equations are extracted from the physical structure of the device containing information about the doping concentrations and electrical terminal characteristics. Generation and recombination rates are calculated based on the defect and impurity densities and external optical illumination rates. Defect and impurity densities are either coupled directly as an estimating input to the device simulations or extracted from process simulation results. Optical generation rate needs to be calculated separately in the optical simulations. The output of the device simulations are the internal distribution of potentials, fields,

and carrier concentrations which provides understating of the device behavior and allows optimization of the device structure and processes.

As a result, in order to develop a predictive TCAD framework process, optical, and device calculations need to be coupled via the continuity equations and all the critical parameters should be calibrated against the experimental measurements.

1.2 PROCESS SIMULATIONS

Process simulations incorporate models used to find the geometrical structure and impurity distributions in the device. The outputs of the process simulation are used as the input of the device simulation, which provide information about internal state of the device. Based on eq. (1.1)-(1.5) process simulation results must contain information about dopant densities, defects distribution, and impurities concentration throughout the device structure.

Currently accurate models on dopant diffusion in the silicon lattice have been developed for arsenic [24], boron [24], and phosphorus [25]. These models accurately capture the impact of dopant/defect pairing and the drift/diffusion of the charged states on the dopant diffusion profiles. In addition, models have also been developed on extended defects in silicon such as dislocation loops and their formation from {311} clusters [27] and oxygen precipitation [28].

The focus of this dissertation in the process calculations is on modeling of the gettering of metal impurities (Cu, Fe, Mo, Ni, and W) and their redistribution in the device structure. These impurities mostly possess deep trap energy levels within the silicon bandgap providing effective generation-recombination centers reducing the yield of the lifetime sensitive devices. Gettering is the common approach to minimize the harm due to these elements to the performance of such devices and involves complex interaction between metals, defects, and the dopants in the system.

Therefore, it was essential to develop predictive models taking all those interactions into account to optimize the gettering processes, as well.

1.3 Optical Simulations

Optical simulations calculate the optical generation rate when an optical wave penetrates into the device and gets absorbed. Optical modeling is essential for modeling optoelectronic devices such as solar cells which are essentially under sun light illumination. The optical simulators model light propagation through the device and based on the properties of the device materials calculate the amount of light absorption and the resulting electron-hole pair generation rate. The simulation results are coupled into the generation term G in eq. (1.2) and eq. (1.3) in the device simulations.

In order to increase the light absorption in the silicon solar cells, the surface of them is textured. The challenge of modeling textured solar cells is related to the fundamental methodology by which simulators solve their models. A grid must first be established on the device structure and then the equations are solved at each grid point. In order to capture the effect of surface texturing on the light absorption, sufficiently fine grids should be established making the simulations take too much memory and CPU time. As a result explicit modeling of textured surfaces within the actual device dimensions requires enormous amounts of grid points and is virtually impossible.

In this work, a hybrid of transfer-matrix-method (TMM) and ray tracing optical modeling is suggested and used to simulate the optical generation rate for textured silicon solar cells within a reasonable simulation time. The critical parameters for optical modeling is calibrated against experimental measurements and excellent results matching the experimental measurements are obtained which proves the accuracy and reliability of the suggested methodology.

1.4 ORGANIZATION OF THIS WORK

Background materials are discussed in Chapter 2. All the models required to solve the device performance equations (Poisson's, electron-, and hole-continuity equations) are discussed and the numerical approaches to solve those equations are presented.

The coupled device and optical modeling of MWT solar cell is discussed in Chapter 3. The process influences on the device performance are extracted based on the experimental measurements and literature. The models are calibrated against the experimental measurements and an excellent basis for performance prediction is developed. Lastly, the opportunities for achieving higher efficiencies are explored in Chapter 3.

Chapter 4 represents the coupled process and device modeling simulations. A predictive and reliable gettering process model is developed. The model involves detailed atomic interaction between impurities and dopants, and crystal defects. In addition, the process simulation results are coupled with the device simulations to model the impact of different annealing conditions on a photodiode device performance.

Lastly, concluding remarks and recommendations for the future works is presented in Chapter 5.

Chapter 2. NUMERICAL MODELING BASICS

This chapter introduces the basic physics governing the silicon devices, and discusses the relevant physical models for generation, and recombination required to solve the electron- and hole-continuity equations introduced in Chapter 1. Subsequently, a short description of solar cell and photodiode performance metrics is presented. Lastly, the chapter ends with a brief review over the methodologies used for solving the device modeling equations.

2.1 FUNDAMENTAL SEMICONDUCTOR CONCEPTS

The common material used in the fabrication of ULSI devices and semiconductor photovoltaics is crystalline silicon. The behavior of electrons in crystalline semiconductor solids such as silicon can be described by the application of quantum mechanics. The most important result of such description is that the allowed energy levels of electrons are grouped into bands which are separated by regions of energy that electrons cannot possess ("band gap" E_g which is 1.12 eV for silicon). The highest energy band that is completely occupied by electrons at 0 K is called the valence band. The next higher energy band, separated by the bad gap from the valence band, is the conduction band. At T > 0K, finite number of electronic states in the conduction band are occupied by electrons (free electrons n) and the left behind empty states in the valance band are called free holes p.

The energy distribution of electrons are governed by Fermi-Dirac statistics the result of which is the Fermi-Dirac distribution representing the probability that an electronic state at energy E is occupied by an electron:

$$f_D(E) = \frac{1}{1+\exp(\frac{E-E_f}{kT})} \tag{2.2}$$

In which k is the Boltzmann's constant and T is the absolute temperature. E_f is called the Fermi level which is the energy at which the probability of occupation by an electron is 0.5.

The equilibrium concentration of electrons and holes can be controlled by extrinsic dopants (donors and acceptors) or by intrinsic defects possessing energy levels within the bandgap and based on that semiconductors are classified as n-type or p-type depending on whether electrons or holes are the majority carries. In semiconductors doped with shallow donors or acceptors, n and p are similar to the donor and acceptor densities respectively.

2.1.1 *Moderately Doped Materials*

In the n-type material that is not too highly doped (nondegenerate), only a small fraction of the allowed states in the conduction band are filled. The Fermi function in the conduction band is very small, and the Fermi level is well below the bottom of the conduction band ($E_C - E_f \gg kT$). As a result, Eq. (2.1) reduces to mathematically simpler Maxwell-Boltzmann distribution function:

$$f_M(E) = \exp(-\frac{E-E_f}{kT}) \tag{2.2}$$

As a result, the equilibrium free electron concentration and the Fermi level are governed by:

$$n = N_C \exp(-\frac{E_C-E_f}{kT}) \tag{2.2}$$

$$N_C = 2(\frac{2\pi m_n{}^* KT}{h^2})^{3/2} \tag{2.3}$$

Similarly, in the moderately doped p-type material, the Fermi level is significantly above the top of the valence band and:

$$p = N_V \exp(-\frac{E_f-E_V}{kT}) \tag{2.4}$$

$$N_V = 2\left(\frac{2\pi m_p{}^* KT}{h^2}\right)^{3/2} \tag{2.5}$$

where N_C and N_V represent effective density of states for the conduction and valence band respectively. In silicon, $N_C = 2.8 \times 10^{19}\ cm^{-3}$ and $N_V = 10^{19}\ cm^{-3}$ at room temperature.

In equilibrium, the product of n and p is constant and depends only on the temperature and is governed by the law of Mass Action:

$$np = {n_i}^2 = N_C N_V \exp\left(-\frac{E_g}{kT}\right) \tag{2.6}$$

In which, n_i is the intrinsic carrier concentration.

2.1.2 *Heavily Doped Materials*

If silicon is doped at densities approaching N_C or N_V, the Maxwell-Boltzmann approximation will not be valid anymore and Fermi-Dirac statistics should be considered. Application of the Fermi-Dirac distribution in the models is most important for many commercial solar cells, as their performance is limited by the regions with $N_{doping} \gg 10^{19}$ [4]. Thus, all the device calculations in this dissertation utilize the Fermi-Dirac statistics.

In addition, as doping densities become a significant fraction of silicon's atomic density ($5 \times 10^{22}\ cm^{-3}$), the original band structure of silicon begins to be perturbed by the interaction of dopants with each other. Each of the dopant atoms adds a discrete energy level close to the edge of the conduction or valence bands, and with high enough densities, the dopant energy levels form another band of energy merging with the conduction or valence bands. Bandgap narrowing is one consequence of such interactions. The reduced band gap causes the np product to increase, which is modeled by:

$$np = {n_{ieff}}^2 = {n_i}^2 \exp(\frac{\Delta E_g}{kT}) \tag{2.7}$$

2.1.3 *Non-Equilibrium*

If we have injection (extra carriers provided electrically) or optical generation (${np > n_i}^2$), or extraction (extra carriers removed electrically, ${np < n_i}^2$), then the system is not in the equilibrium and Eq. (2.2) and (2.4) cannot represent the carrier concentrations, as Fermi level is meaningless. However, quasi-Fermi levels E_{fn} and E_{fn} can be defined to replace the Fermi level E_f so that similar carrier density equations hold under steady-state:

$$n = N_C \exp(-\frac{E_C - E_{fn}}{kT}) \tag{2.8}$$

$$p = N_V \exp(-\frac{E_{fp} - E_V}{kT}) \tag{2.9}$$

The quasi-Fermi levels are mathematical tools and their values are chosen so that we can extend our familiar equilibrium equations to non-equilibrium situations. As a result, $|E_{fn} - E_{fp}|$ is the measure of the extent to which the semiconductor is away from the equilibrium:

$$np = {n_{ieff}}^2 \exp(\frac{E_{fn} - E_{fp}}{kT}) \tag{2.10}$$

We will find the concept of the quasi-Fermi levels useful when we discuss the numerical simulation methods.

2.2 GENERATION-RECOMBINATION

Recombination is the mechanism which re-establishes the thermal equilibrium as the system enters in the non-equilibrium situations. The focus of this section is on the indirect semiconductors such as silicon and germanium in which the minima of conduction band does not occur at the same point in momentum space as the maxima of the valence band. As a result, in order for excess carriers to recombine, simultaneous three-particle (electron, hole and a phonon) interaction is required. Three-particle interactions are far less likely to happen than two-particle interactions (electron and hole) taking place in the direct semiconductors. However intermediate localized electronic states, introduced by defects intrinsic to the silicon lattice or extrinsic impurities such as metals, capable of trapping both electrons and holes can act as stepping stones and turn the three-particle interaction process into a two-particle interaction process, hence more likely to happen.

Electronic traps exists both in the bulk of the semiconductors and at the surfaces. The recombination mechanism taking place via the traps in the bulk of the semiconductors is called bulk recombination and is modeled by Shockley-Read-Hall (SRH) recombination equation and the recombination via surface traps is called surface recombination and is modeled by surface SRH recombination equation, and in the simplified form is modeled by a surface recombination velocity.

2.2.1 *Shockley-Read-Hall Recombination*

The generation-recombination rate associated with each trap is modeled by [5]:

$$U = \frac{N_t v_{th} \sigma_n \sigma_p (np - {n_{ieff}}^2)}{\sigma_p \left[p + n_{ieff} \exp(\frac{E_i - E_t}{kT})\right] + \sigma_n \left[n + n_{ieff} \exp(\frac{E_t - E_i}{kT})\right]} \tag{2.11}$$

$$= \frac{(np - {n_{ieff}}^2)}{\tau_{n0} \left[p + n_{ieff} \exp(\frac{E_i - E_t}{kT})\right] + \tau_{p0} \left[n + n_{ieff} \exp(\frac{E_t - E_i}{kT})\right]} \tag{2.12}$$

In which,

$$\tau_{n0} = \frac{1}{N_t v_{th} \sigma_n} \tag{2.13}$$

$$\tau_{p0} = \frac{1}{N_t v_{th} \sigma_p} \tag{2.14}$$

Where N_t represents the trap density, and $\sigma_n$and σ_p represent electron- and hole- capture cross sections associated with the trap respectively.

If $(np > {n_i}^2)$, Eq. (2.11) is positive and we have net recombination, however, if $(np < {n_i}^2)$ the sign changes and there is a net thermal generation.

The SRH recombination-generation U is maximum if the trap energy level is near the middle of the bandgap. As a result impurities with deep energy levels contribute the most to the total bulk recombination-generation in the device and shallow traps have the least contribution.

Under low-level injection, a condition under which the external disturbance does not appreciably change the total free carrier density from its equilibrium value ($\Delta n \ll N_d \; and \; \Delta p \ll N_a$), Eq. (2.11) reduces to:

$$U = \frac{\Delta n}{\tau_n} \tag{2.15}$$

for p-type regions, and:

$$U = \frac{\Delta p}{\tau_p} \tag{2.16}$$

for n-type regions. Therefore, the recombination rate depends only on the lifetime of the minority carriers, and hence the name minority carriers' lifetime.

Total generation-recombination is strongly due to all of the existing impurities and defects and is the sum of the recombination rates by each individual trap:

$$U = \sum_i U_i \tag{2.17}$$

$$\frac{1}{\tau} = \sum_i \frac{1}{\tau_i} \tag{2.18}$$

Therefore, details of the distribution of all of the defects and impurities throughout the entire device is required to calculate Eq. (2.17). This goal is partly achieved in this dissertation by modeling of the redistribution of five transition metals Fe, Cu, Ni, Mo, and W. Modeling of the other types of defects and impurities has not been in the focus of this job and therefore for modeling of metal-wrap-through solar cells the impact of various traps are absorbed in the lifetime model and the critical parameters were calibrated against the experimental measurement.

Most of the silicon wafers used in the VLSI technology, are prepared by Czochralski (Cz) process. High purity silicon is melted in a silica (SiO_2) or quartz crucible at just above the silicon melting point (1417℃) [14], and then a small single-crystal seed mounted on a rod is lowered into the melt. The crystalline orientation of the silicon wafers is determined by the orientation of this seed. In addition some amount of dopant is placed in the crucible to dope the wafers. Then the seed is slowly pulled out of the melt and the resulting ingot will be diced into wafers. The high temperature of the process also incorporates the oxygen from the crucible into the melt and wafers.

In boron doped melts, the incorporated oxygen atoms bind with the boron dopants and form BO_2 complexes that can act as very effective recombination centers [45]. Therefore, the electron carrier lifetime in such boron-doped wafers is strongly dependent on density of boron and oxygen in the silicon. Fig. 2.1 demonstrates the dependence of the measured electron lifetime of a Cz-Si boron-doped wafers on the density of the boron concentration.

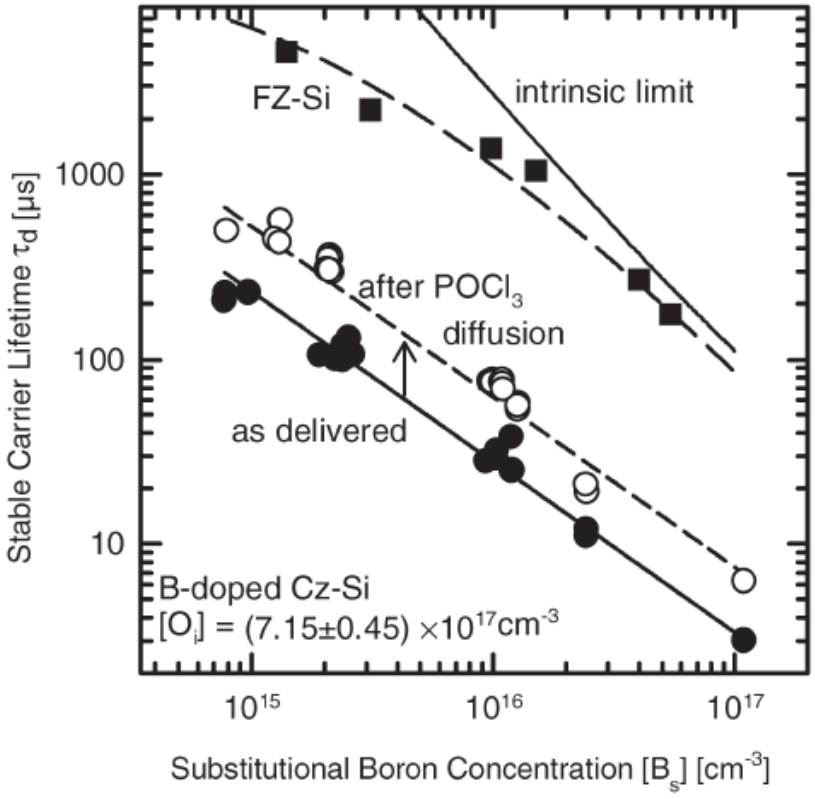

Figure 2.1. Electron lifetime of boron doped Cz-Si wafers vs. substitutional boron concentration. Reproduced from Ref. [45].

In this dissertation, for simulations of metal-wrap-through (MWT) solar cells, such dependence is modeled by:

$$\tau_{bulk} = \frac{\tau_0}{1+(\frac{N_{boron}}{N_{ref}})^{\gamma}} \tag{2.19}$$

In which, the parameters N_{ref} and γ capture the dependence of the bulk lifetime on the boron content, and the impact of the rest of the impurities in the wafer on the lifetime is absorbed in τ_0 so that the bulk lifetime matches the experimental measurements. The models parameters, extracted from the literature and experimental measurements is listed in Table 2.1.

Table 2.1. Bulk Lifetime Model Parameters for Cz-Si Boron-Doped Wafers.

Parameter	Value
$\tau_0{}^{\text{electron}}$	550.25
$\tau_0{}^{\text{holes}}$	183.43 ms
N_{ref}	1.5×10^{13} cm^{-3}
γ	1

2.2.2 *Surface Recombination*

Incompletely bonded silicon atoms at the surface can provide efficient traps of recombination. Even though, the density of the dangling bonds can be significantly reduced by passivating the surface with oxide [46], surface states still provides generation-recombination centers in addition to those present in the bulk. The surface recombination is modeled by:

$$U_{surface} = S\Delta n \tag{2.20}$$

where S is defined as the surface recombination velocity. The surface recombination velocity is experimentally measured and coupled into the device modeling.

2.2.3 *Optical Generation*

In addition to electrical injection, the carrier concentration in the device can also be disturbed by light illumination. If the energy of the incident photon is larger than the bandgap of the semiconductor, the covalent bonds holding the electrons in the valence band can be broken and

the excited electrons and the resulting left behind holes can both contribute to the electrical current of the device. This process is called photo or optical generation. The bandgap of silicon is 1.12 eV which is energetically equivalent of photons with wavelength of 1.2 μm. As a result, silicon used in the photovoltaic devices is capable to have photocurrent generation from solar radiation within wavelengths no larger than 1.2 μm.

Based on the optical properties of the surface layer deposited on a silicon wafer, some portion of the incident photon is absorbed at the surface and the rest is reflected. This absorption rate is of significant importance for solar cells as the goal is to maximize the cell efficiency as much as possible. Thus, a layer of anti-reflective-coating (ARC) which is often a single layer of SiO_2 or Si_3N_4 is deposited on top of all commercial silicon solar cells. In addition the top surface of them is also textured, so as to at least two attempt to enter the silicon wafer is achieved by each light beam. Fig. 2.2 is a schematic of a silicon textured surface visualizing the concept of surface refection improvement.

The light is then absorbed as it penetrates into the wafer. The amount of light absorption in small increments of length is wavelength dependent and is described by an absorption coefficient α shown in Fig. 2.3 for different semiconductors. The intensity of the light at the depth x below the incident surface is modeled by:

$$I(x) = I_0 \exp(-\alpha x) \tag{2.21}$$

where I_0 is the intensity of the light beam entering the silicon lattice. The goal of an ARC layer is to maximize I_0. The optical generation rate is also modeled by:

$$G(x) = \alpha N_0 \exp(-\alpha x) \tag{2.22}$$

where N_0 is the number of photons of the light entering the silicon lattice.

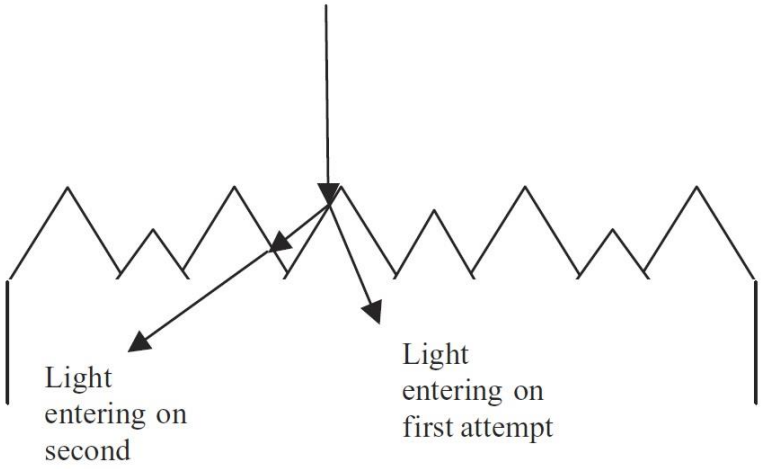

Figure 2.2. Schematic of a textured surface demonstrating the possible paths a light beam can enter the silicon wafer. Reproduced from Ref. [43].

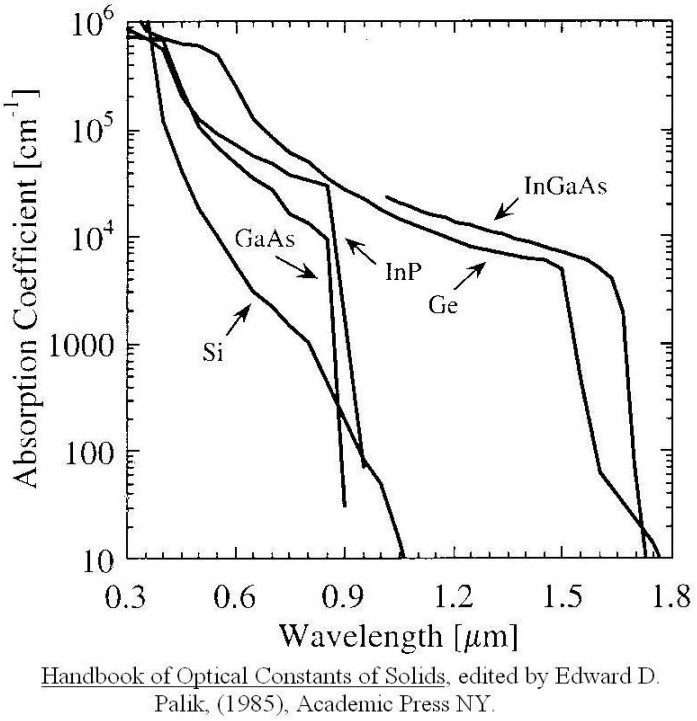

Figure 2.3. Absorption coefficient of light vs. wavelength for different semiconductors. Reproduced from Ref. [47].

Solar cells are illuminated by the sun light which is caused by blackbody radiation from the outer layer of the sun. Fig. 2.4 shows the sun light spectrum (am1.5 [3]) at top of the atmosphere (used on satellite's solar cells) and at the see level (used on the commercial solar cells). The total photo-generation in the wafer is then calculated by integrating Eq. (2.22) over the wavelengths of the sun light spectrum:

$$G_{ph} = \sum_{\lambda} \alpha N_0 \exp(-\alpha x) \tag{2.23}$$

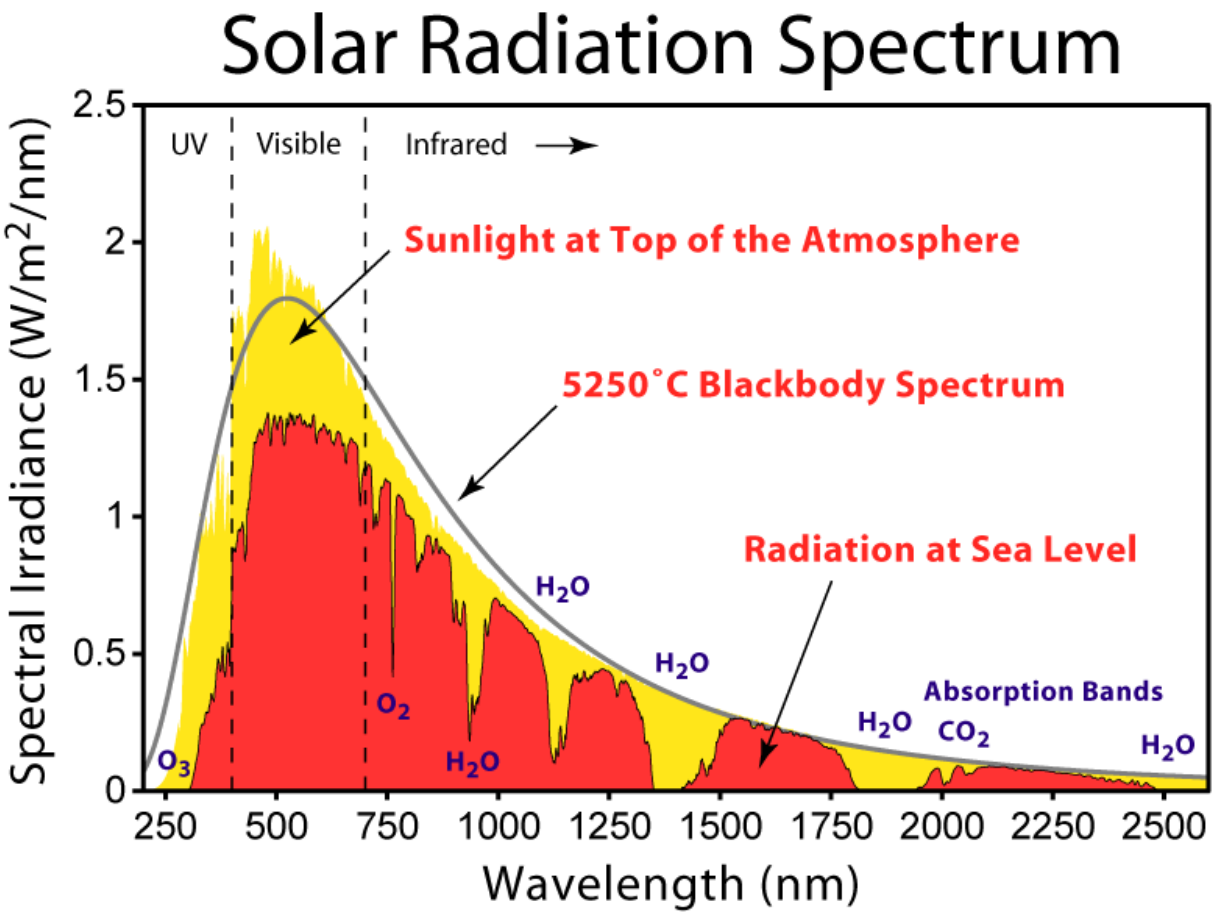

Figure 2.4. Solar radiation spectrum at top of the atmosphere and at the sea level. Reproduced from Ref. [44].

In this dissertation, in order to conduct optical modeling within a reasonable computation time accurately, ray-tracing method [2] is used to model the light absorption and the resulting optical

generation rate from the sun light spectrum. The impact of the ARC layers is also modeled by transfer-matrix-method (TMM) [2] suitable for optical modeling of layered planar structures. FDTD method [2] is the most accurate and versatile modeling approach, however due to dimensions of the commercial solar cells, it requires large amount of gridding nodes (explained in the next chapters) and thus memory and CPU time.

2.3 Solar Cell and Photodiode Device Performance

Solar cells and photodiodes are fundamentally P-N junctions which are under light illumination. The generated electron-hole pairs in the depletion region of the P-N junction, drift across the depletion region and enter the p- and n-type regions as majority carriers and end up as photo-generated current. The photo-generated current flows in a direction opposite to the foreword bias current of the P-N junction. It is also possible for minority carriers, generated within one diffusion length from the edges of the depletion region, to diffuse and reach the depletion region and get swept across by the space charge field and end up as photo-generated current. As a result, it is necessary to minimize carrier recombination (maximize the diffusion lengths of minority carriers) to allow carriers deliver their energy to external circuits. The photo-generated current density can be estimated as:

$$J_{ph} = q \int_{-x_p - L_n}^{x_{n+L_p}} G_{ph} \tag{2.23}$$

in which, $-x_p$ is the location of the depletion region edge in the p-type region, x_n is the location of the depletion region edge in the n-type region, L_p is the holes' diffusion length in the n-type region, and L_n is the elections' diffusion length in the p-type region of the diode.

The difference between solar cells and photodiodes, is in their electrical region of operation. Solar cells operate in forward bias to deliver energy, however photodiodes operate in reverse bias.

Fig. 2.5 compares the I-V characteristics of a solar cell and a photodiode with and without illumination.

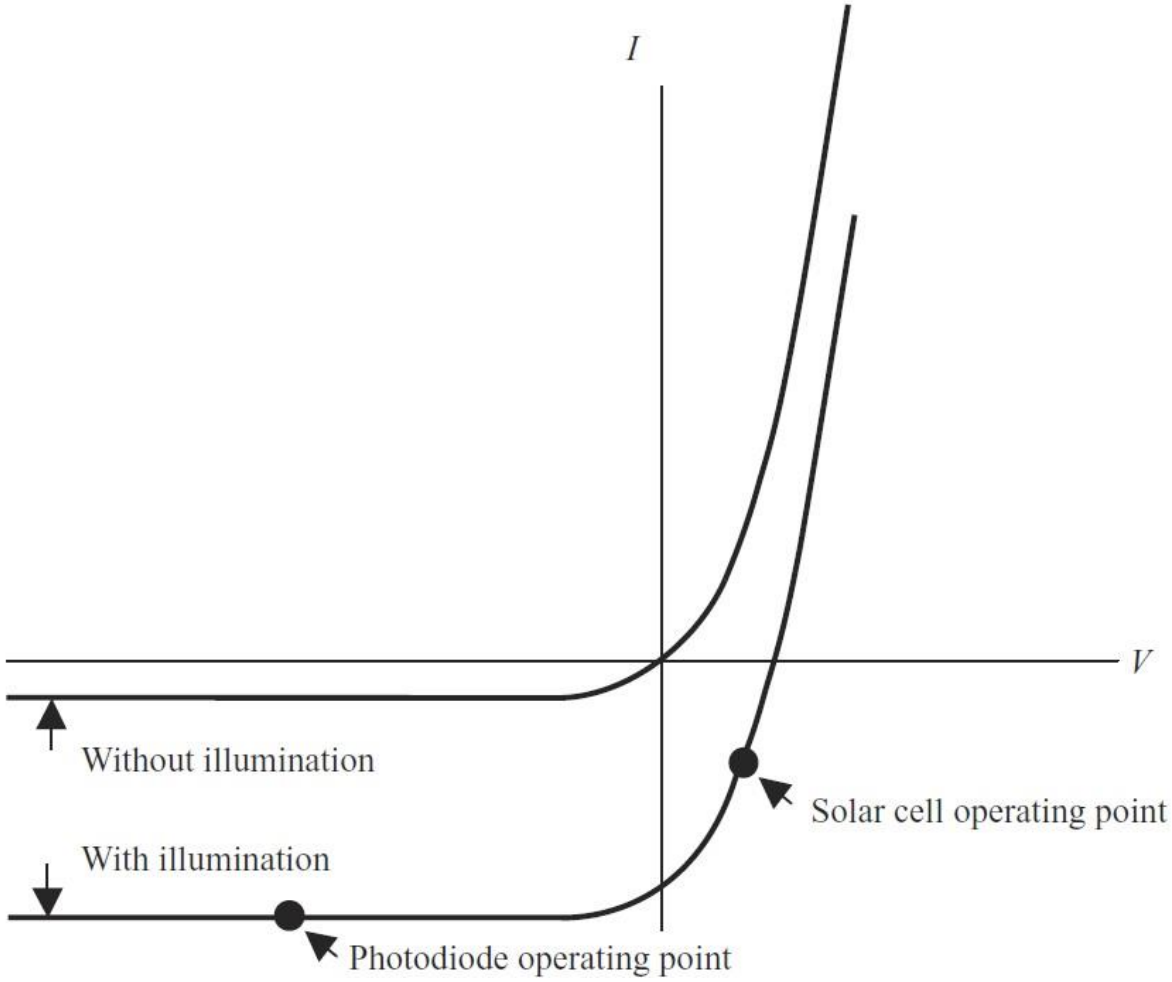

Figure 2.5. The I-V characteristics of a solar cell or a photodiode with or without illumination. Reproduced from Ref. [43].

Based on the equation modeling an ideal diode's J-V characteristics and Eq. (2.23), the total current of ideal solar cells and photodiodes can be modeled as:

$$J = J_0 \left(\exp\left(\frac{q(V - JR_s)}{kT} \right) - 1 \right) - J_{ph} \tag{2.24}$$

In which J_0 is the saturation current density of the diode, and R_S is the lumped series resistivity (Ωcm^2) of the diode accounting for all the resistive losses.

Based on Eq. (2.24), the performance metrics of photodiodes and solar cells can be defined. These definitions are required for understanding the concepts represented in Chapters 3 and 4 on modeling of the MWT solar cell and the photodiode.

The *short circuit current density* (J_{sc}) of a solar cell is the amount of current delivered in zero voltage bias ($V = 0$). Hence,

$$J_{sc} \cong J_{ph} \tag{2.25}$$

The *open circuit voltage* (V_{oc}) of a solar cell is the voltage found by setting $I = 0$ in Eq. (2.24):

$$V_{oc} = \frac{kT}{q} \ln\left(\frac{J_{ph}}{J_0} + 1\right) \tag{2.26}$$

The *maximum power point (MPP)* is the operating point of a solar cell at which the product of current and voltage of the device (delivered power) in fourth quadrant operating region is maximum, and from that *Fill Factor* (FF) is defined as:

$$FF = \frac{V_{mp} J_{mp}}{V_{oc} J_{sc}} \tag{2.27}$$

Finally, the *efficiency* (η) of the solar cell is defined as:

$$\eta = \frac{V_{mp} J_{mp}}{P_{light}} \tag{2.28}$$

in which P_{light} is the total power of the incident light.

The *dark current* of a photodiode is defined as the current that the diode at reverse bias and under no light delivers:

$$J_{dc} = J_0 \tag{2.29}$$

As the reverse voltage of the photodiode increases, the depletion region of the diode gets wider and the reverse current of the diode in dark conditions is dominated by the thermal generation within the depletion region, hence the need for a mechanism redistributing the traps away from the P-N junctions where the depletion regions are located. Such mechanism is called gettering and is modeled in detail in Chapter 4. With long-base diode assumption, the dark current is modeled by:

$$J_{dc} = q{n_i}^2\left(\frac{D_p}{N_d L_p} + \frac{D_n}{N_a L_n}\right) + q\int_{-x_p}^{x_n} U \tag{2.30}$$

$$= q{n_i}^2\left(\frac{D_p}{N_d L_p} + \frac{D_n}{N_a L_n}\right) + q\,\frac{n_i}{2\tau_0}\,{x_d}' \tag{2.31}$$

where N_d and N_a are the doping concentrations of the n-type and p-type regions respectively, and ${x_d}'$ which is dependent on the reverse bias voltage, is the portion of the depletion region width over which Eq. (2.11) is maximum [48]. In deriving Eq. (2.31), it is also assumed that $\sigma_n = \sigma_p$, so that $\tau_0 = \tau_{p0} = \tau_{n0}$ in Eq. (2.13) and (2.14). The first term in Eq. (2.30) is related to generation in the quasi-neutral regions near the depletion region and the second term is due to generation in the depletion region. Table 2.2 summarized the defined parameters.

Table 2.2. Basic Solar Cell and Photodiode J-V Performance Characteristics.

Parameter	Symbol	Unit
open circuit voltage	V_{oc}	mV
short circuit current density	J_{sc}	mA/cm^2
maximum power point	P_{max}	mW/cm^2
fill factor	FF	%
efficiency	η	%
dark current	J_{dc}	pA/cm^2

2.4 BASICS OF THE NUMERICAL MODELING

As explained in the introduction chapter, the electrical characteristics of the electronic devices are predicted by solving the Poisson's, electron- and hole-continuity equations (Eq. (1.1)-(1.3)). In this work only steady-state solutions to the equations are investigated:

$$\frac{\partial n}{\partial t} = 0 \tag{2.32}$$

$$\frac{\partial p}{\partial t} = 0 \tag{2.33}$$

The recombination terms R in Eq. (1.1) and (1.2) have nonlinear dependency on the carrier concentrations n and p Eq. (2.11). As a result, Eq. (1.1)-(1.3) represents a set of nonlinear partial differential equations which are solved by the typical methodology: (1) establishment of a grid (meshing) superimposed on the device geometry, (2) discretization of the equations at each node of the grid, (3) application of the boundary conditions (terminal characteristics), and (4) solving the resulting matrix equation over the nodes by iteration. The solutions consists of three state variables ϕ, E_{fn} and E_{fp} from which all other variable are calculated in the steady-state.

2.4.1 *Grid Setup*

Numerical solutions are based on calculating physical properties at a number of nodes which are intersection points of a grid superimposed on the device structure. Grid generation in two- and three-dimensional structures is one of the challenging tasks in the device simulations as they must be fine enough to capture details of interest, yet coarse enough without requiring excessive computation time. The grid spacing must be consistent with the expected structural and electrical variations.

In typical device simulators, a non-uniform rectangular grids are initially established so that the nodes can be concentrated in the regions with abrupt changes in doping. The coarse rectangular grid is the refined and converted to a triangular grid by adding diagonals until it is fine enough to represent the structure accurately. In addition the simulators can automatically redistribute the grid points to improve the accuracy during the simulation (e.g. based on abrupt changes in potential). Fig. 2.6 shows a triangular grid applied on a piezo-resistive (PZR) sensor.

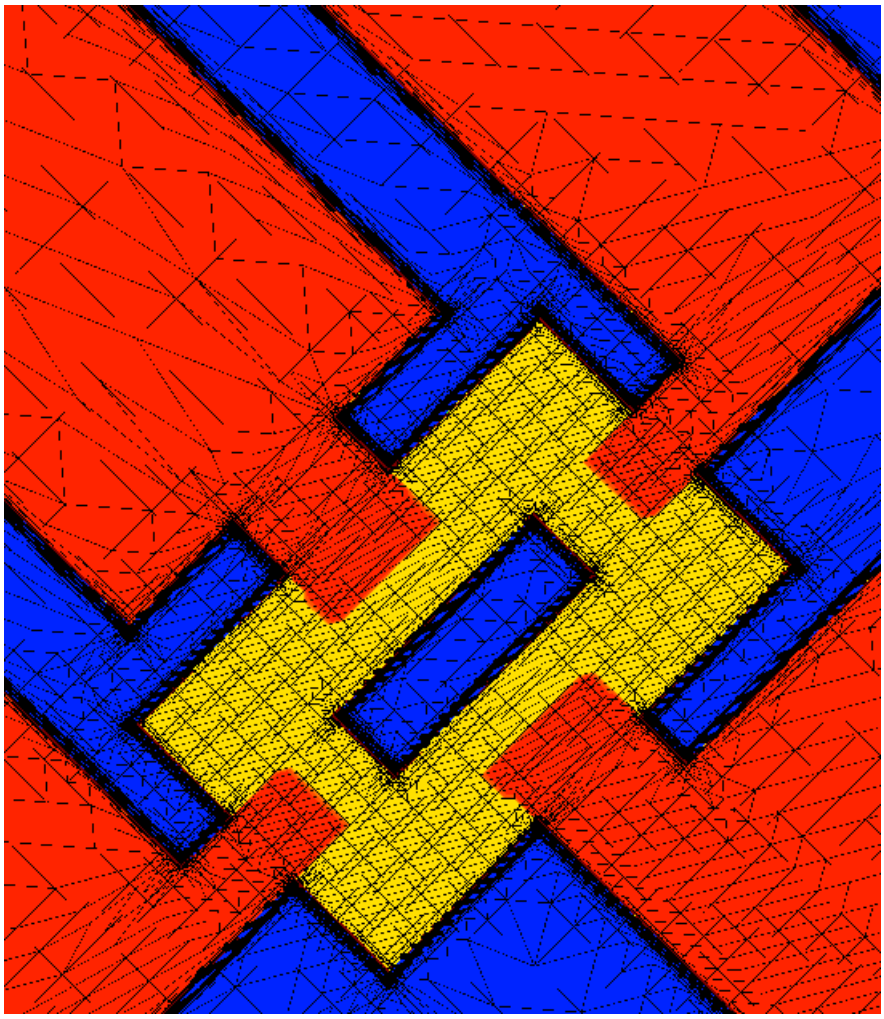

Figure 2.6. Application of a triangular mesh on a PZR sensor device structure for numerical modeling.

2.4.2 *Discretization of Equations*

After the establishment of the grid, three equations (Eq. (1.1)-(1.3)) will be associated with each grid node. The simulator solve the three partial differential equations self-consistently for potential ϕ, and electron and hole quasi-Fermi potentials E_{fn} and E_{fp}. The carrier densities n and p are then calculated form the quasi-Fermi potentials in the steady-state. However, the continuous differential equations must first be discretized by converting them to difference equations at each node. Each node represent the small volume surrounding it and the behavior of each node primarily depends on immediately surrounding nodes. The net flux of charge entering the volume is considered, along with generation-recombination sources inside it, to conserve charge and current. The current is calculated along each line segment of each triangle, and the potential gradient (electrical field from which the drift flux of carriers is calculated) along each line segment is the difference in the potentials at the two points divided by length of the line segment connecting them.

Solutions to the set of 3N coupled nonlinear difference equations (Poisson's and n- and p-continuity equations at N grid points) are obtained by nonlinear iterations starting from an initial guess made based on the solution for zero bias, or a previous solution for slightly different bias. In this dissertation, Newton's method has been used in the simulations in which all the variables are allowed to change during each iteration and the coupled algebraic difference equations are solved at the same time by matrix inversion. Because the potential, electron and hole quasi-Fermi potentials are considered simultaneously, the matrix which is inverted in Newton's method is 3N×3N requiring large memory and long computation time for complex devices.

2.4.3 *Boundary Conditions*

In addition, boundary conditions at the interfaces between different materials in the device structure must be specified. Typical boundary conditions used in the device simulations are ohmic,

Schottky, insulating, and reflecting boundary conditions. In ohmic contacts the electron and hole quasi-Fermi potentials are fixed at the applied voltages and no space charge exists. This is a good approximation for metal contacts made on heavily doped regions in which carriers can easily tunnel through the Schottky barriers. In this dissertation ohmic contacts along with a surface recombination velocity are defined at the metal contacts to the silicon. Schottky contacts are defined by the work function difference between the electrode metal and the semiconductor and are usually used when the Schottky diode and the space charge associated with it is being modeled. Insulating boundaries, such as oxide layer of MOS transistors, are described by a work function which determines the surface potential. Reflecting boundaries are used at non-contacted edges of the device so that the normal current to those boundaries is zero.

Chapter 3. COUPLED OPTICAL AND DEVICE MODELING OF TEXTURED MWT SILICON SOLAR CELLS

Currently, wafer-based crystalline solar cells are the dominant photovoltaic technology in industry. However, to continue to move down the historical experience curve for the module price index [1], improved manufacturing efficiencies will not suffice. Cell performance enhancement and a reduced bill of materials will be required to meet US Department of Energy's module cost target of 0.50 USD/Wp by 2020. We explored a simplified hybrid of a metal-wrap-through (MWT) and laser-fired-contact (LFC) design to achieve greater than 20% cell efficiency on a p-type monocrystalline silicon substrate at the cost target. A simplified cross sectional view of the proposed device structure is shown in Fig. 3.1. The purpose of this dissertation is to establish an accurate TCAD framework to efficiently develop both understanding and prediction of the cell performance for a given device structure. As a result, the cell architecture and process recipe influences can then be tuned to maximize the cell efficiency.

As stated in the introduction, the performance simulation of optoelectronic devices can be divided into 3 sub-tasks: process simulation to predict detailed device structure, optical simulation to predict light propagation and absorption in the structure, and device simulation to predict final output characteristics. The focus of this work is on the optical and device simulations; and the process influences on the structure and boundary conditions have been extracted and coupled into the calculations either from experimental measurements or based on the literature. Due to the geometry of the structure, it was critical to conduct the simulations in 3D in order to capture the impact of the vias, the metal-wrap-through bus bar, and the base contacts on the cell performance. The impact of the surface texturing has been modeled in the optical simulations and at the end the

simulation results of the baseline model have been backed up by the experimental characterization data from sample devices fabricated in the lab from which simulations were developed.

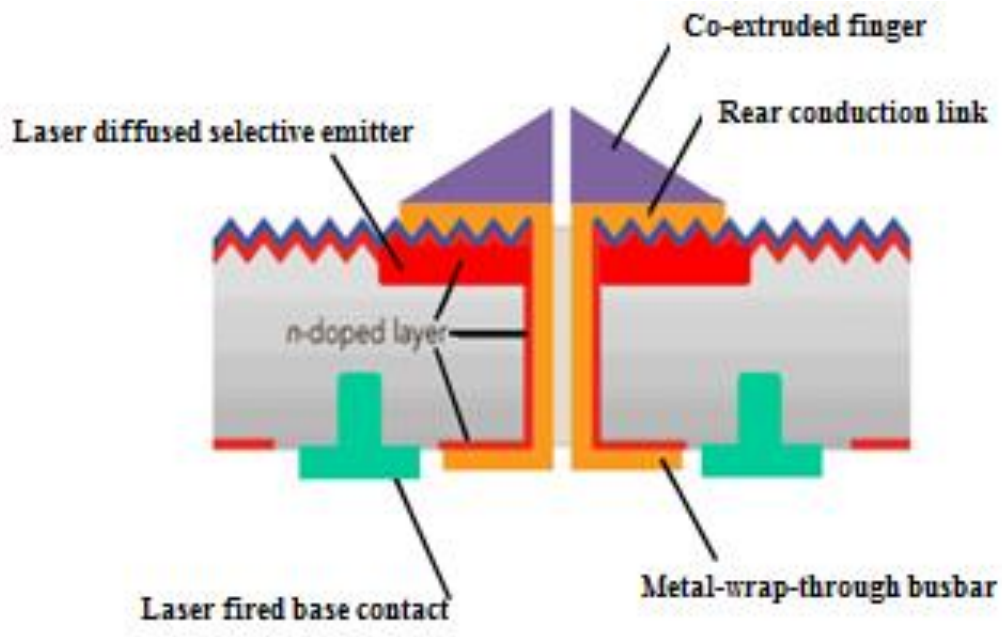

Figure 3.1. Schematic of proposed device architecture employing a selective emitter metal wrap through, laser fired contact solar cell on thin, p-type, Cz-Si substrates.

3.1 Optical Simulation

3D optical simulations for textured surfaces were done within the Sentaurus Device Platform [2] using the ray-tracing method, with the transfer matrix method used to model the impact of antireflective coatings. The input spectrum used to simulate optical generation rate within the structure was am1.5 [3]. When performing 3D simulation for textured solar cells, the optical modeling and electrical calculations need to be performed separately due to the different length scales. The typical dimensions of a pyramid within a textured surface is on the order of a few microns; whereas, the length of one period of the MWT cell is on the order of a millimeter. Therefore, it is almost impossible to explicitly model textured solar cells directly, because, it would

demand too much memory and CPU time. As a result, the optical simulation was done on a small system which includes only one pyramid. In order to link the optical simulation result of the small textured surface to the actual structure's dimensions, the reflection spectrum of a wafer with flat surface and textured surface were calculated; and based on Eq. (3.1), the intensities of the original input spectrum were modified so that the post processed input spectrum would produce the same light absorption, and optical generation in a system with a flat surface.

$$I_{Flat}^{PostProcessed}(\lambda) = \frac{1-R_{Textured}(\lambda)}{1-R_{Flat}(\lambda)} I_{Textured}(\lambda) \qquad (3.1)$$

In Eq. (3.1), $1 - R(\lambda)$ is the transmission coefficient of each surface type, and I is the intensity of the incident light as a function of wavelength. Thus, by using the post processed spectrum, the same amount of light is transmitted into the bulk which produces the same optical generation.

3.1.1 *Simulation Setup*

The structure used in the optical simulation of the textured surface is a 180 μm thick wafer with 5 μm by 5 μm lateral dimensions with pyramidal texture on the top surface. The optical boundary conditions are chosen reflective at the front, back, left, and right sides of the structure which effectively makes the system a wafer with a periodic array of pyramids. A single layer anti-reflective coating is applied on top of the pyramid, and the back side reflection is chosen constant. In addition, the impact of a randomly textured surface on the light reflection is simulated and compared to the one of the pyramidal texture. Fig. 3.2 shows the top pyramid structure used for the optical simulation compared to a randomly textured surface and Fig. 3.3 compares the simulated reflections of the two surface types. As can be seen, due to the large lateral dimensions of the system compared to the range of the wavelengths of the input spectrum, there is a negligible difference between the simulated reflections, and as a result, a pyramidal texture with reflective

boundary conditions could accurately capture the impact of texturing on the optical generation rate through the wafer.

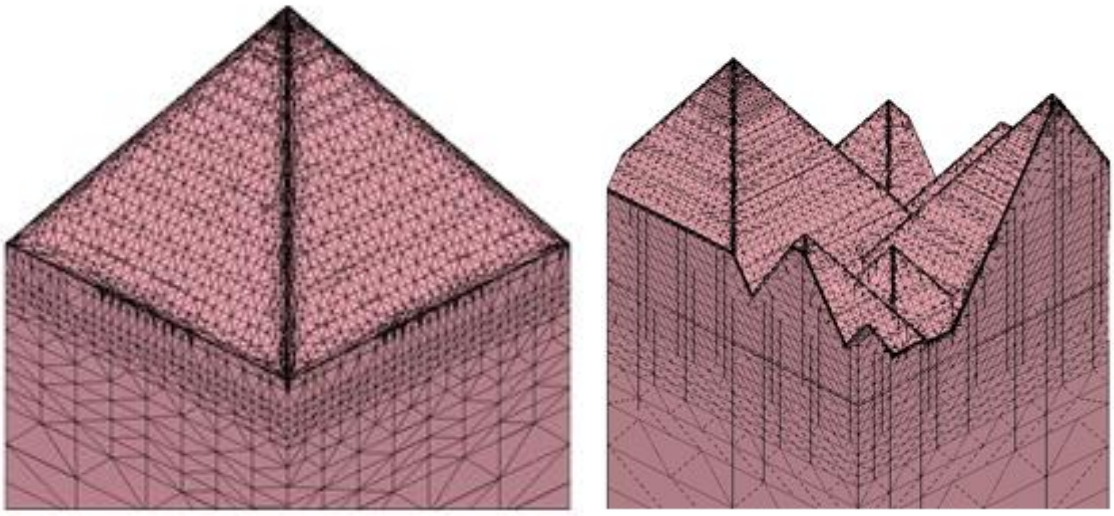

Figure 3.2. Optical simulation setup and grid of textured surfaces.

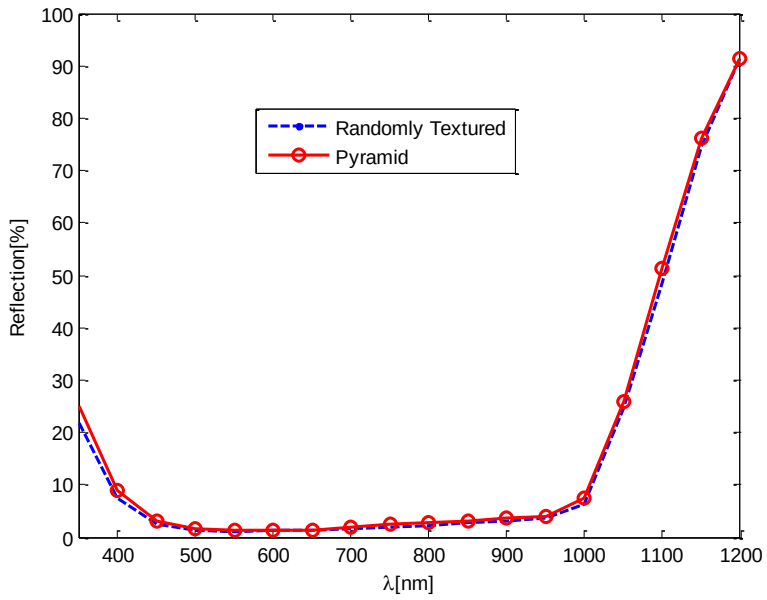

Figure 3.3. Simulated reflection of a wafer with pyramidal texture compared to the simulated reflection of a randomly textured wafer.

3.1.2 *Calibrations and Results*

The dielectric constant and thickness of the top surface anti-reflective coating are tuned to match the measured reflection spectrum of a wafer without back side metallization. The result is shown in Fig. 3.4. Similarly, the back side passivation thickness and material was tuned to match the measured back side reflection spectrum, as shown in Fig. 3.5. Based on that, the back side reflectivity was chosen to match the reflection off the front side of the wafer with the same dielectric passivation at the rear side. We found that a constant reflectivity over all frequencies (99.5%) was sufficient to match the measured data.

After these calibrations, the calculated front side reflection of the flat and textured surfaces are plugged into Eq. (3.1), to give the input spectrum to be used in the simulations. Fig. 3.6 compares the simulated front side reflection of the flat and textures surfaces and Fig. 3.7 compares the original input sun light spectrum and the post processed one calculated by Eq. (3.1).

In order to validate this methodology, the post processed and the original input spectrums have been simulated on a flat and a textured solar cell, respectively. The solar cells had the same doping concentrations and dimensional characteristics, shown in Table 3.1, except for the different top surface texture. Fig. 3.8 compares the simulated internal quantum efficiency of each cell under the stated different illuminations. The results are in good agreement between the two cases with maximum error less than 7% and error in the total optical generation rate of less than 2%, demonstrating the effectiveness of the approach. The error in the optical generation rate due to each wavelength was also less than 2%.

This methodology only matches the optical generation rates at each wavelength; however, since the short circuit current also depends on the geometry of the cells, some modest differences remain.

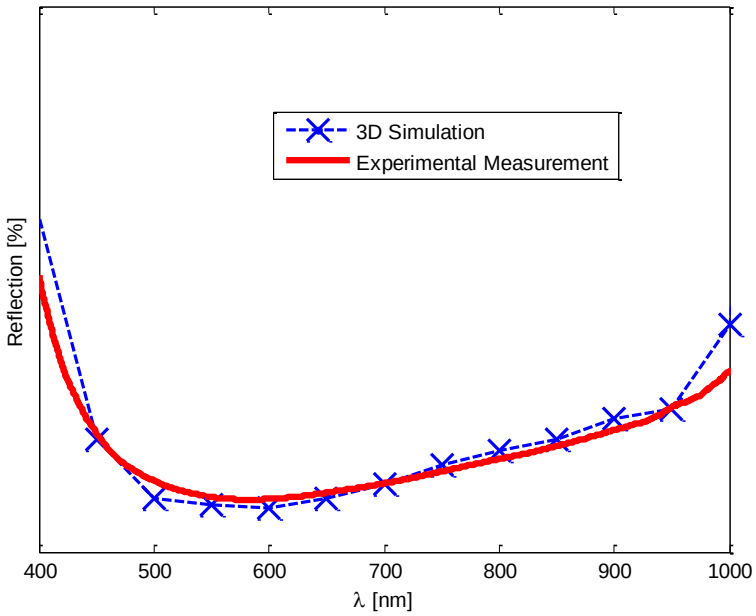

Figure 3.4. Simulated reflection of a wafer without backside metallization compared to the measured reflectance spectrum (experimental values are proprietary, so y-axis values are not shown).

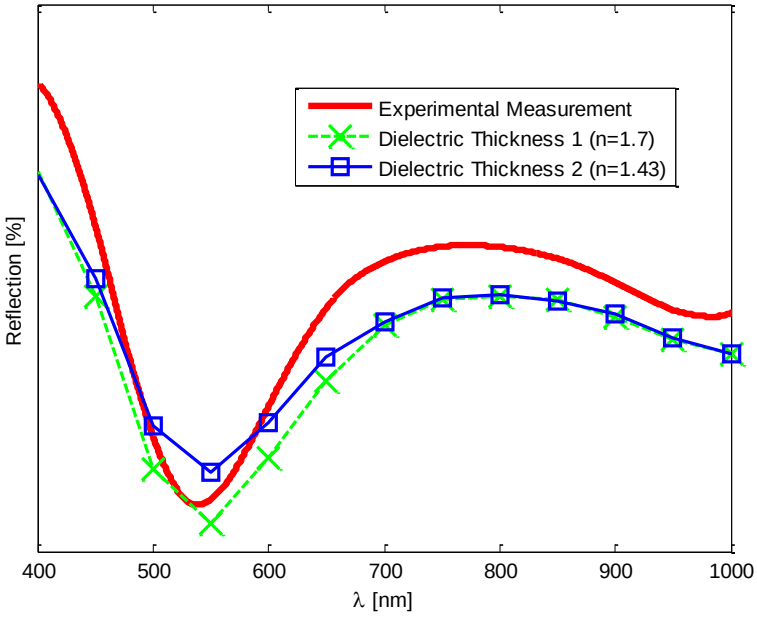

Figure 3.5. Simulated reflection of the wafer with different dielectric passivation compared to measured reflectance spectrum (experimental values are proprietary, so y-axis values are not shown).

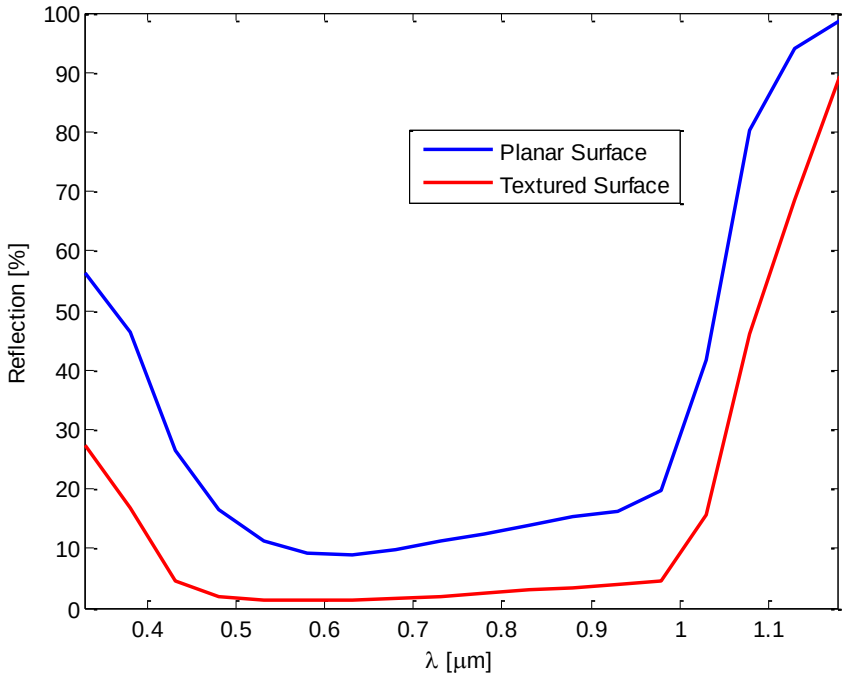

Figure 3.6. Simulated front side reflection of a flat surface compared to the reflection of a textured surface.

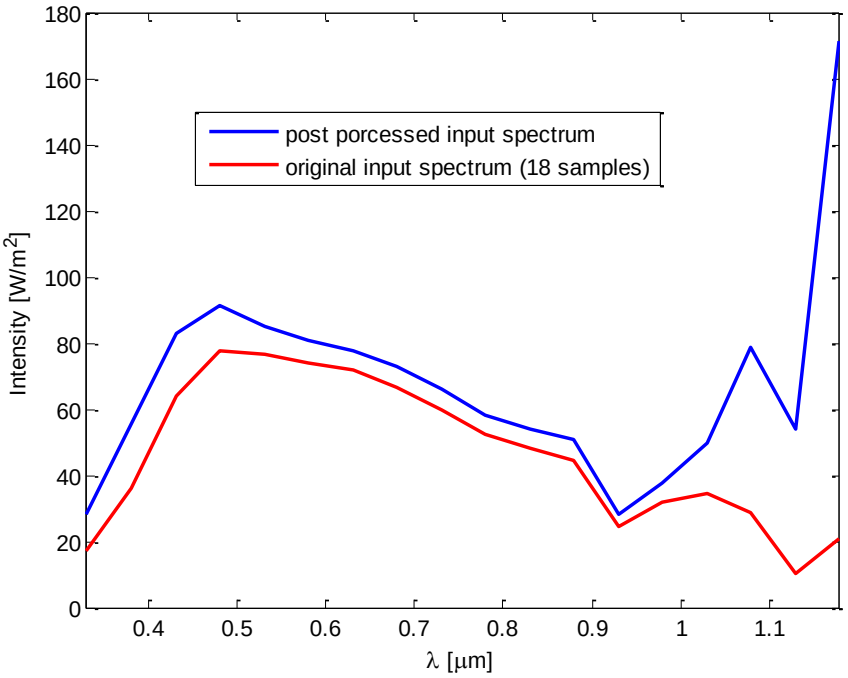

Figure 3.7. Original input (am1.5) and modified spectrums.

Table 3.1. Solar Cell Device Structure Parameters Used in the Internal Quantum Efficiency Simulations.

Parameter	value
Wafer Thickness	180 μm
Wafer Width	5 μm
Bulk Doping Concentration (Uniformly Doped)	3.3×10^{16} cm^{-3}
Front Emitter Peak Doping Concentration (Gaussian)	5.44×10^{20} cm^{-3}
Front Emitter Junction Depth	0.2 μm

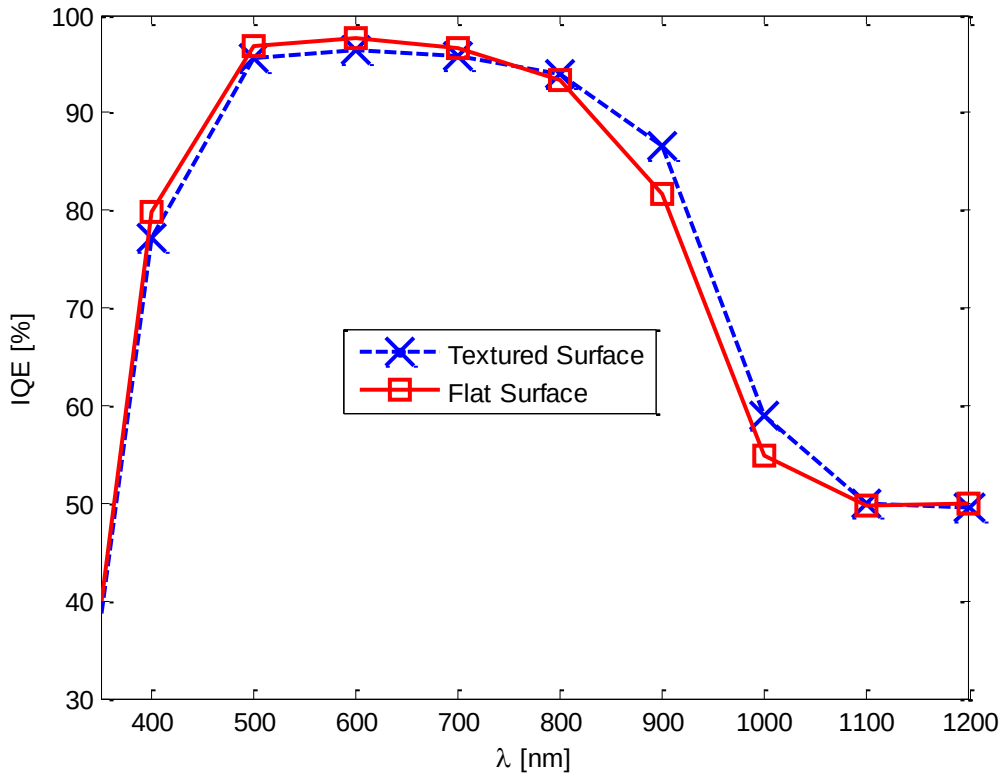

Figure 3.8. Simulated internal quantum efficiencies of the textured and flat solar cells illuminated by am1.5 and modified spectrums, respectively.

3.2 DEVICE SIMULATIONS

The p-type MWT structure was constructed in the dimensions of the measurement samples. Due to the symmetry and periodicity of the structure, the simulations were only done on one fourth of a period of the full device, so as to minimize CPU memory usage and simulation time. The phosphorus and aluminum doping concentrations of the front emitter and back-surface-fields respectively were directly taken from electrochemical-capacitance-voltage (ECV) measurements. Fig. 3.9 shows the front and back side views of the structure used in the device simulation.

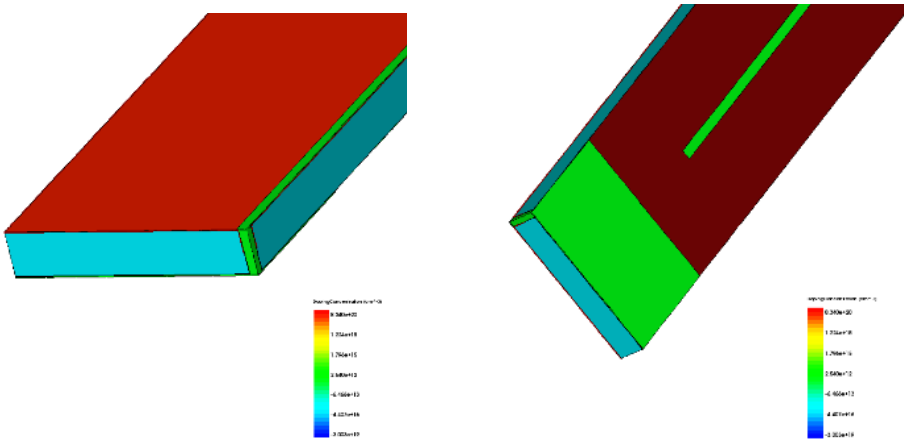

Figure 3.9. One quarter of a period of the MWT silicon solar cell structure. The metallization is shown in green, and the n-type and p-type doping are shown in red and blue, respectively. The backside passivation is shown in brown (The left picture shows the front emitter doping and top fingers and the right picture depicts the back side passivation, bus bar, and the back-surface-field (BSF) fingers).

3.2.1 *Device Simulation Models*

The carrier mobility is modeled as by Masetti [4] (Appendix A) with the Del Alamo band gap narrowing model [4] taken into account. Defect recombination in the bulk and at the surfaces are

modeled with the Shockley-Read-Hall (SRH) model [5]-[7]. The parameters of the bulk SRH model (bulk minority carriers' lifetime) are extracted from Quasi-Steady-State (QSS) and Quasi-Transient (QT) Photo-Conductance Decay (PC) [8]-[12] measurements done on bifacial passivated emitter doped samples. The photo conductance decay methods measure the effective carrier lifetime of the samples which is affected by all sources of carrier loss (recombination) throughout the device and can be modeled by:

$$\frac{1}{\tau_{eff}} = \frac{1}{\tau_{bulk}} + \frac{2J_{oe}(N_a+\Delta n)}{qn_i^2 W} + \frac{2x'_d\sqrt{\frac{N_a+\Delta n}{\Delta n}}}{(\tau_n+\tau_p)W} \tag{3.2}$$

In which, τ_{bulk} is the wafer minority carriers' lifetime, τ_n and τ_p ate electron and hole bulk lifetimes respectively, x'_d is the width of the depeletion region at p-n junctions over which SRH recombination is maximum, J_{oe} is the emitter saturation current, N_a is the bulk doping concentration, Δn is the excess minority carrier concentration, and W is the wafer thickness. Fig. 3.10 compares the QSSPC and QTPC measurements against which Eq. (3.2) is calibrated.

Auger recombination is taken into account using standard values for silicon [5]. The via metal and top finger resistivities were taken from the experimental measurements, and the back surface field metallization resistivity and contact resistance were extracted based on the literature [13] and modeled as a lumped series resistance to be calibrated for matching the simulated Fill Factor (FF) to the measurement. The major contribution to this series resistance is from the base contact resistance which is proportional to the base effective specific contact resistivity (ρ_c) and inversely to the base contact area.

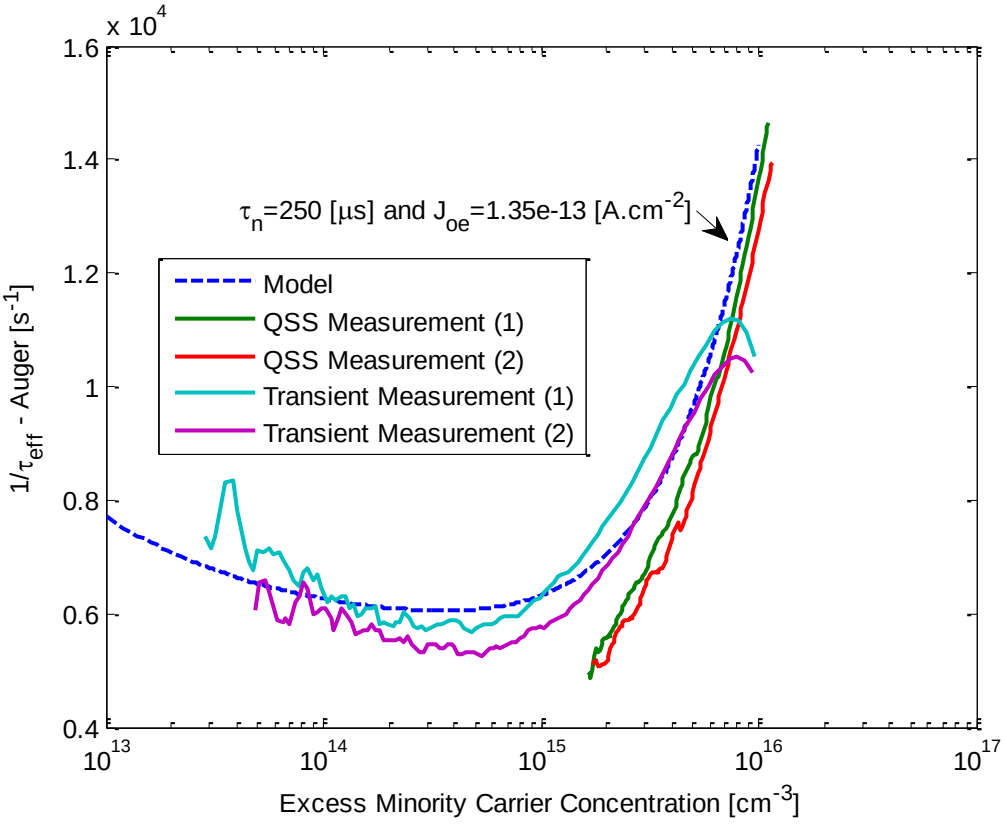

Figure 3.10. Bulk minority carrier lifetime and emitter saturation current extraction based on Eq. (3.2) and Quasi-Steady-State and Quasi-Transient Photo-Conductance Decay measured versus injection level.

3.2.2 *Simulation Results*

Based on the stated calibrations and models, excellent match to the measured device behavior has been achieved. The comparison is given in Table 3.2. The experimental values were measured and averaged from 13 samples. Opportunities for device optimization have been investigated through geometrical optimization, improvement of the wafer minority carriers' lifetime, the quality of the backside passivation dielectric and also the specific contact resistivity of the aluminum paste used for making the base fingers doping and metallization. In the following figures, the efficiency values are relative to baseline and the baseline conditions (zero relative efficiency) are geometrical and boundary conditions of the experimental samples used in the measurements.

Table 3.2. Comparison between Simulation and Measurements.

	J_{sc} [mA/cm^2]	V_{oc} [mV]	FF [%]	P_{max} [mW/cm^2]
Simulation	38.84	659	75.9	19.44
Experiment (Average)	38.95	650	75.8	19.2

The top fingers are fabricated by co-extrusion gridline printing technology. The spacing between fingers (emitter finger pitch) was already optimized in the technology based on the emitter sheet resistance and top finger resistivity, as confirmed by simulations. Thus we have only plotted the impact of the via pitch (the spacing between the via holes) on the cell efficiency. The result is shown in Fig. 3.11. As the via density gets larger (smaller via pitch), there is a lower peak photo generated current passing through the top fingers which reduces the voltage drop along the top fingers. On the other hand, because the bus bar metallization width and the gap between the bus bar and base fingers remains constant, with smaller via pitches (higher via densities) the ratio of base finger area to the backside passivated area gets smaller. As a result, the base contact resistance increases with degradation in FF at higher via densities. Partially compensating, the reduced back contact area does lead to slightly increased Voc and Jsc as via density increases. Fig. 3.11 demonstrates the tradeoff between the top finger and base contact resistances and their impact on the Fill Factor and efficiency of the cell with respect to via density.

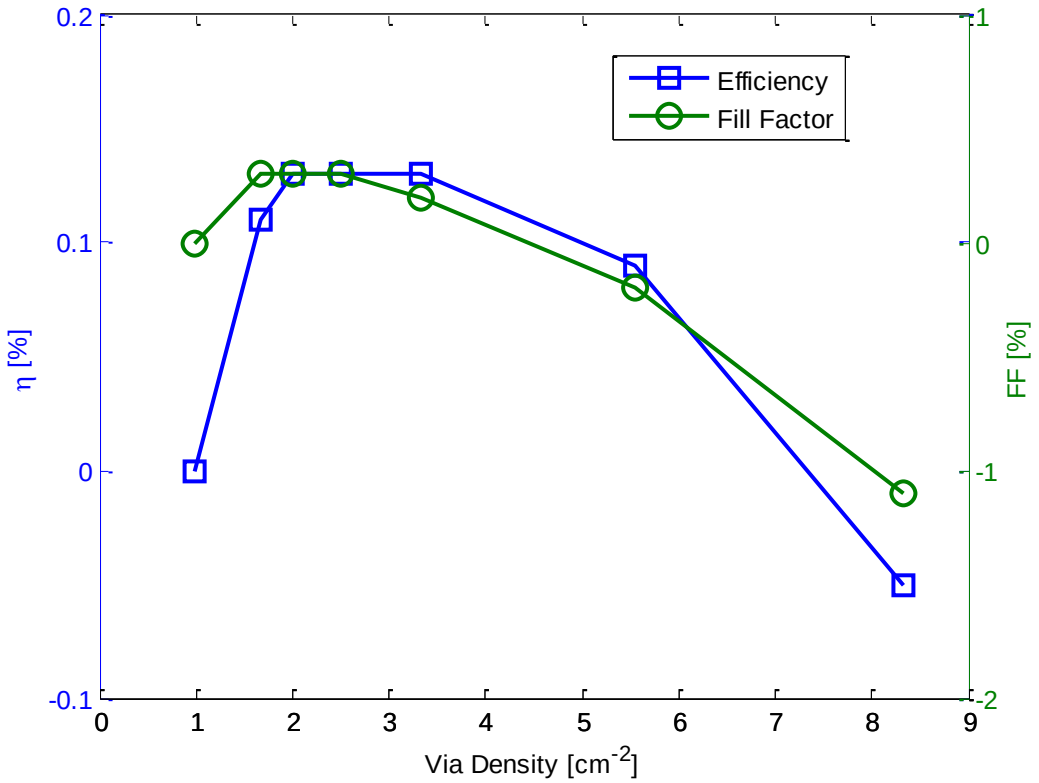

Figure 3.11. Simulated efficiency and Fill Factor vs. via density (efficiency and fill factor values are relative to baseline).

Fig. 3.12 shows simulated relative efficiency as a function of backside surface recombination velocity for two different specific base contact resistivities. As shown in the figure, the efficiency of the solar cell is a strong function of backside passivation quality, i.e. the back side surface recombination velocity and base contact resistance. Better quality of passivation leads to higher open circuit voltage and lower base contact resistivity leads to higher Fill Factor and thus higher efficiency. The main contributor to the base series resistance is the base contact resistance which could be reduced by either using a paste with lower specific contact resistivity or by increasing the base contact width. Fig. 3.13 shows the simulated cell efficiency as a function of base width. While a wider base contact has less associated series resistance, it also causes more recombination losses,

reducing the short circuit current and open circuit voltage of the cell. Thus, there is an optimum base width of about 150 µm, which balances these issues.

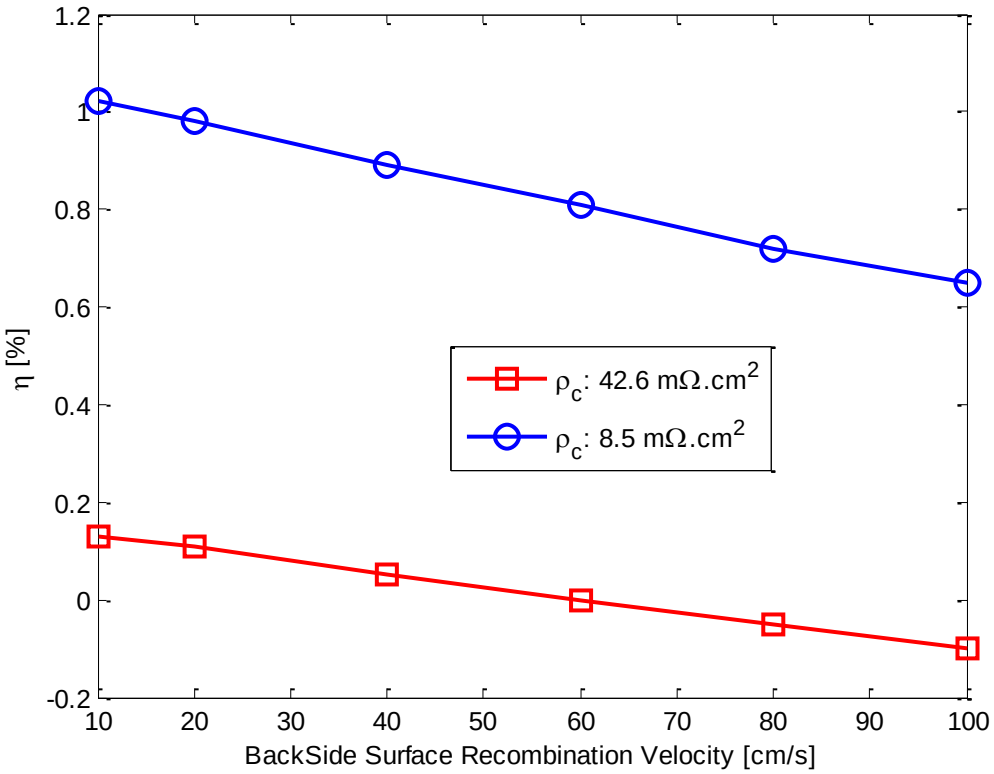

Figure 3.12. Simulated efficiency vs. backside surface recombination velocity (efficiency values are relative to baseline).

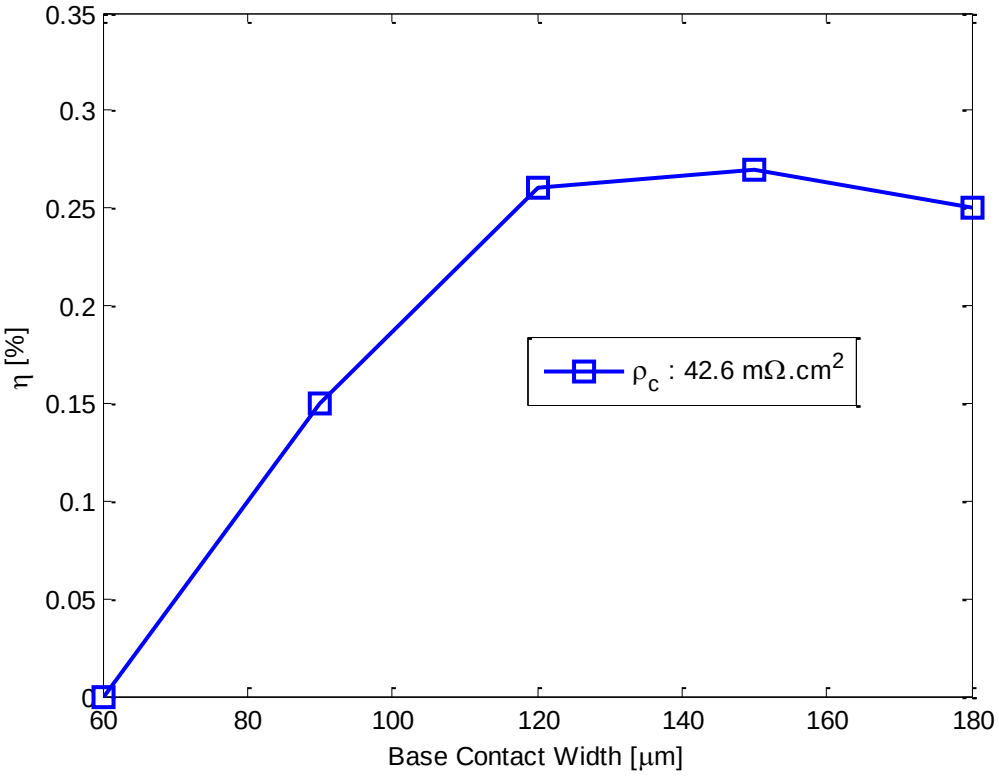

Figure 3.13. Simulated efficiency vs. base contact width (efficiency values are relative to baseline).

The dependence of the cell efficiency on the minority carrier lifetime of the wafer has also been simulated and is shown in Fig. 3.14. There is limited improvement in the performance of the device by using wafers with higher carrier lifetimes, as the cell performance is limited by back surface passivation.

The simulation results clearly identify the most effective options for cell efficiency improvement. Most effective would be the use of a base contact paste with a substantially reduced specific contact resistivity (+0.8% gain). Some of the latter gains can be achieved by increasing the base contact area, but the gains are much more limited (+0.27%) due to associated increase in back side recombination and resistive losses. Other significant enhancements in efficiency would

come from increasing the via density, improving the back side passivation (reduction of the surface recombination velocity) and using wafers with higher bulk lifetimes, each of which gives on the order of a 0.1% absolute boost in cell efficiency.

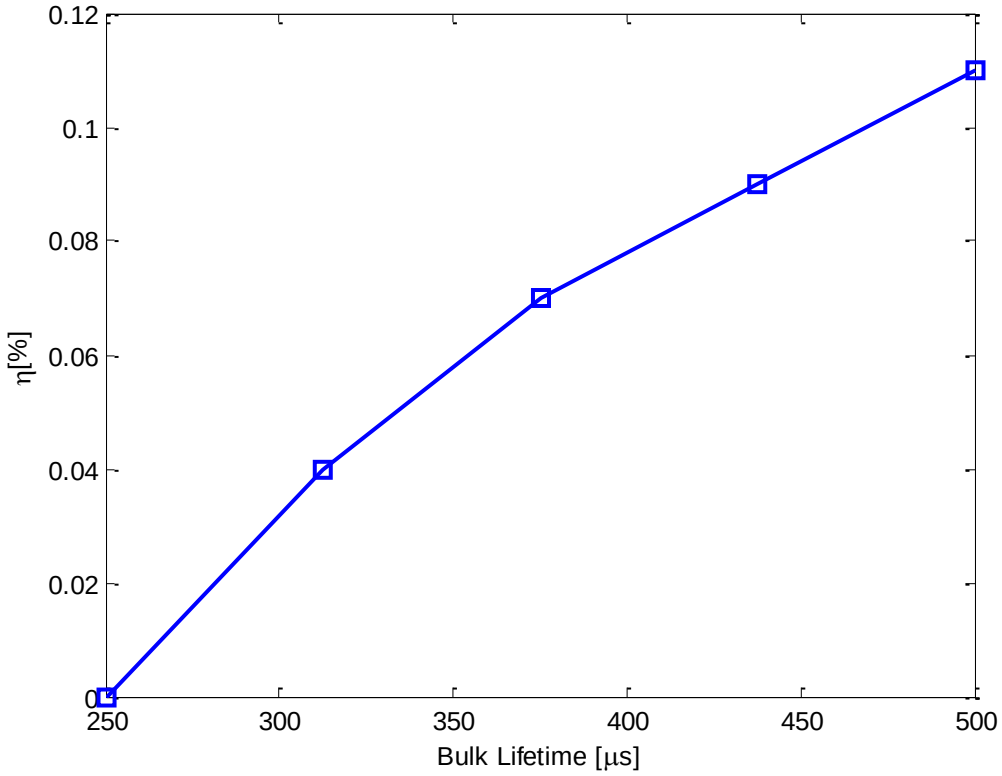

Figure 3.14. Simulated efficiency vs. bulk lifetime (The values are relative numbers).

3.3 SUMMARY

This dissertation illustrates the potential of TCAD simulations for optimizing an advanced solar cell process. 3D simulation were done on a metal wrap-through solar cell with local laser-fired back contacts The effect of the textured surface has been included in the optical simulations. All the models and parameters were calibrated based on the experimental measurements or the literature. Excellent match to the sample measurements has been achieved, and a good basis for

optimization has been developed. Moreover, the most significant opportunities to achieve higher efficiencies were identified.

Chapter 4. COUPLED MODELING OF THE GETTERING OF TRANSITION METALS AND PERFORMANCE OF LIFETIME-SENSITIVE DEVICES

Metal impurities dissolved in silicon wafers such as Fe, Cu, Ni, W and Mo often possess deep energy levels within the silicon bandgap providing effective generation-recombination centers and have detrimental impact on the performance of optoelectronic devices such as solar cells and CMOS image sensors. These generation-recombination centers result in reduction of carrier lifetime and thus reduction in the efficiency of solar cells and also increasing the junction leakage current of CMOS image sensors. Many of these metals are fast diffusers with diffusivities many orders of magnitude larger than common dopants [14] and, as a result, in the same time that dopants are diffusing to form P-N junctions, metals can easily diffuse and redistribute throughout the whole wafer. Gettering is the common approach to minimize the harm due to these elements in both solar cells and CMOS image sensors by taking advantage of the high diffusivity of transition metals and removing them from the active device region and trapping them in the gettering sites to which they are preferentially attracted. It is therefore essential to develop investigative and predictive models incorporating important atomic processes in gettering to explore various processing conditions for optimum gettering and overall device efficiency in a cost effective manner. However, current VLSI TCAD tools do not have sufficient models for the gettering processes, and previous research has mostly focused on modeling of gettering of iron and insufficiently on other metals [15]-[20].

In this work we combine *ab initio* and continuum approaches to model gettering of the five mentioned transition metals to phosphorus and boron doped regions, as well as to dislocation loops formed from {311} clusters and oxygen precipitates in silicon wafers. The ab initio calculations are performed to determine the binding energy of metals to the mentioned gettering sites and then

continuum models are built to simulate kinetics of trapping of these metals by the gettering sites simultaneously with the diffusion and clustering of the dopants and the metals. Finally, the process simulation results are coupled with device simulation through Shockley-Read-Hall (SRH) recombination model [5]-[7] to predict the impact of gettering on the performance of lifetime sensitive devices. The result demonstrates an effective approach to predict device performance based on processing conditions and the initial impurity distribution in the wafer. Fig. 4.1 shows a schematic of the TCAD system developed in this work.

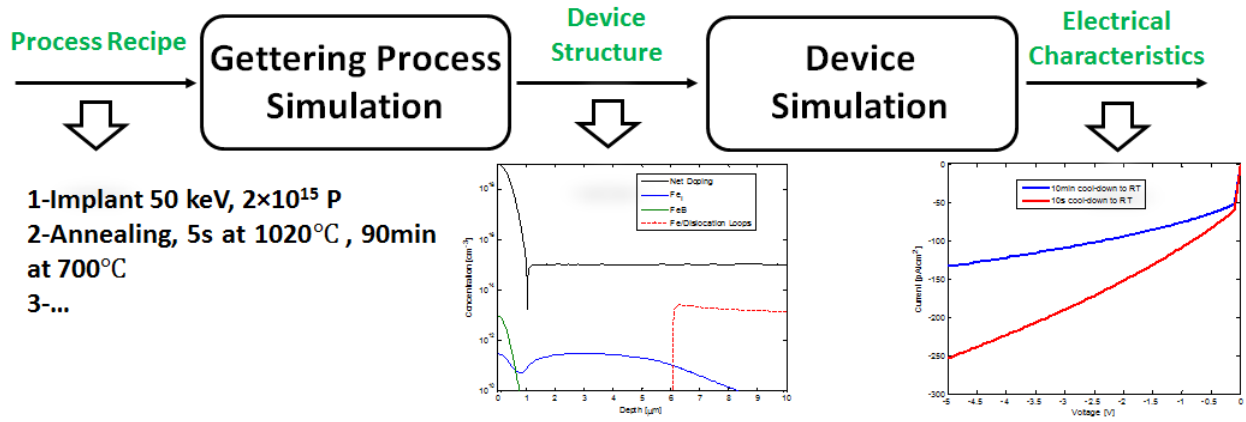

Figure 4.1. Schematic of the developed TCAD system for performance simulation of lifetime sensitive devices based on the initial impurity content.

4.1 Detailed Process Models

All the *ab initio* calculations were done using the density functional theory (DFT) code VASP [21]-[22]. DFT calculations of the binding energy of transition metals to the gettering sites used a 64-atom supercell with energy cutoff of 340 eV and 2^3 Monkhorst k-point sampling method with generalized gradient approximation (GGA). The continuum models are developed from the binding energies calculated by DFT and are implemented within Sentaurus Process Platform via the Alagator scripting language [23]. In addition to gettering continuum models, 5-stream models for boron [24] and phosphorus [25] diffusion have been implemented in Sentaurus. The models

accurately capture the impact of the dopant/defect pairing, and the drift/diffusion of charged states on diffusion profiles. In addition, a high concentration diffusion model is taken into account for P [53]. P_4V complex formation model [26] have been taken into account for heavily phosphorus doped regions which accurately models the phosphorus deactivation and immobilization. P_4V clusters also serve as gettering sites for transition metals. Dislocation loop formation models from {311} defects [27] and oxygen precipitation [28] in silicon have also been included providing another important gettering sites for transition metals.

4.1.1 *DFT Calculations of Energetics of Metal Binding to Gettering Sites*

Binding energy of interstitial metals to the substitutional dopants, phosphorus-vacancy clusters, and dislocation loops are calculated by DFT and shown in Table 4.1. More negative energies in the table indicate more binding to the specified site. As a result, in comparison with dislocation loops and phosphorus-vacancy clusters there is modest binding between metals and substitutional boron and no significant binding to substitutional phosphorus in the phosphorus doped emitters which, as a result, is neglected in our continuum calculations. In addition, the binding energy of metals to point defects are also calculated and shown in Table 4.2. As can be seen, there is a slight binding between most metals and interstitials and slight repulsion between W and interstitials, whereas there is a strong binding between all metals and vacancies. However, due to the large formation energy of vacancies (3.5 eV) and interstitials (3.7 eV) the number of metal-vacancy and metal-interstitial pairs are generally negligible compared to other complexes.

Table 4.1. Binding Energy of Interstitial Metals to Different Gettering Sites Calculated by DFT in VASP.

Metal	Binding to B_S [eV]	Binding to P_S [eV]	Binding to P_4V [eV]	Binding to Dislocation Loops [eV]
Cu	-0.41	-0.04	-2.41	-0.82
Fe	-0.52	-0.02	-1.57	-1.85
Mo	-0.48	0	-1	-1.07
Ni	-0.51	-0.1	-1.93	-1.19
W	-0.56	0.07	-1.50	-1.5

Table 4.2. Binding Energy of Interstitial Metals to Point Defects.

Metal	I [eV]	V [eV]
Cu	-0.21	-3.19
Fe	-0.18	-1.53
Mo	0	-2.09
Ni	-0.46	-1.66
W	0.04	-2.35

4.1.2 *Continuum Models for Metal Redistribution and Gettering*

To model the redistribution of metals within the silicon, drift and diffusion equations are used, based on Eq. (4.1) and Eq. (4.2):

$$J_{diff} = -D_{Metal}\nabla(C_{Metal}) \tag{4.1}$$

$$J_{drift} = -\frac{kT}{q} D_{Metal} C_{Metal^+} \nabla\left[ln\left(\frac{n}{n_i}\right)\right] \tag{4.2}$$

$$C_{Metal^+} = \left[\frac{\exp(\frac{E_{Metal}-E_i}{kT})(\frac{n_i}{n})}{1+\exp(\frac{E_{Metal}-E_i}{kT})(\frac{n_i}{n})}\right] C_{Metal} \tag{4.3}$$

In which, E_{Metal} is the energy levels of each metal within the silicon bandgap, shown in Table 4.4, and E_i is the intrinsic fermi level. Metals are mostly stable in the tetrahedral interstitial sites in the silicon lattice with concentration of C_{Metal} and are mobile with diffusivity D_{Metal} described by:

$$D_{Metal} = D_0 exp(\frac{-E_a}{kT}) \tag{4.4}$$

The pre-factor D_0 and the activation energy E_a for diffusion of each metal are listed in Table 4.3.

Table 4.3. Measured Diffusivity of Metals in the Silicon Lattice.

Metal	D_0 [cm^{-2}/s]	E_a [eV]	Ref.
Cu	0.0047	0.43	[48]
Fe	0.0013	0.68	[49]
Mo	0.26	2.2	[50]
Ni	0.002	0.47	[51]
W	2.68×10^{-5}	2.39	[52]

Continuum models describing metal gettering in the silicon lattice have been built based on DFT calculations and can simply be described by the reactions:

$$Metal + B \Leftrightarrow Metal/B \tag{4.5}$$

$$Metal + P_4V \Leftrightarrow Metal/P_4V \tag{4.6}$$

$$Metal + DL \Leftrightarrow Metal/DL \tag{4.7}$$

In which, DL is the dislocation loops formed by oxygen precipitation or {311} cluster evolution. With the assumption that each reaction is diffusion limited, the reaction rates are defined as:

$$R_{Metal/S} = 4\pi a D_{Metal}\left(C_{Metal}C_S - K_{eql}^{Metal/S}C_{Metal/S}\right) \quad (4.8)$$

$$K_{eql}^{Metal/S} = \gamma . C_{Si} . exp(\frac{E_{Binding}}{kT}) \quad (4.9)$$

In which, S is the gettering site (e.g. boron, P_4V clusters, and dislocation loops) with concentration of C_S, $C_{Metal/S}$ is the concentration of metal trapped by gettering site S, and a is the capture radius of the reacting species with typical value of 0.5nm. $E_{Binding}$ is the binding energy between metals and the gettering site S shown in Table I, and γ is related to entropy change during binding. Its value was optimized to achieve minimum difference between SIMS and simulated Fe during binding between Fe and P_4V clusters in [26] and as a reasonable approximation, the same value is used for pairing reactions related to W and Mo as well. It is also optimized for Cu and Ni to minimize the difference between simulation and SIMS measurements extracted based on the literature [31]. The calibrated values of γ used in the simulations are listed in Appendix B.

Thus the rate of change of the concentration of each metal in the silicon lattice as a function of time is governed by:

$$\frac{\partial C_{Metal}}{\partial t} = -\nabla \cdot \left(J_{Metal}^{diff} + J_{Metal^+}^{drift}\right) - R_{Metal/B} - R_{Metal/P_4V} - R_{Metal/DL} \quad (4.10)$$

In addition, a trapping model for phosphorus dopant at silicon and SiO_2 interface [29]-[30] is also included to simulate the dose loss of phosphorus due to segregation at Si/SiO_2 interfaces.

4.1.3 *Verification of the Gettering Models*

To verify the models, we have performed a simulation under the same conditions reported in [31] on an n-type monocrystalline Si wafer, oxidized to form silicon dioxide on the surface with thickness of 5nm. The wafer was contaminated with Cu, Fe, and Ni with dose of 2×10^{14} atoms/cm^2 and then was annealed at 950℃ for 10min after contamination; as a result, in the simulations it is assumed that the metals are distributed uniformly within the wafer. Given the diffusivity of metals and the length of the initial diffusion step, this is a sound and justifiable assumption. After that the wafer was ion implanted with phosphorus at 50 keV and with dose of 5×10^{15} atoms/cm^2 and then annealed at 1020℃ for 5s and 700℃ for 90min. It was observed that Ni and Cu were trapped within 50nm below the surface while Fe was trapped slightly deeper around 100nm below the surface.

The damage distribution caused by ion implantation is modeled by Monte Carlo simulations [32]. With this dose and energy of phosphorus ions, ion implantation drives the silicon amorphous within a range of 100nm below the surface which is regrown back to crystalline structure by solid phase epitaxy after annealing [14]. As a result within that range no initial interstitial super saturation exists leading to less dopant diffusion and {311} cluster formation. Fig. 4.2–4.4 compare the simulated phosphorus diffusion and calibrated metal redistribution models with the respective SIMS profiles. The simulation results are in good agreement with the experimental measurements and clearly identify the most important kinetic phenomena for gettering processes causing the different observed responses from Fe versus Cu and Ni. As can be seen from Table 4.1 and the simulation results, Ni and Cu have larger binding energy to P_4V clusters and are trapped within about 60 nm below the surface, which is the region of highest phosphorus and P_4V concentration, whereas Fe has larger binding energy to dislocation loops and is trapped around 100 nm below the surface, where end-of-range dislocation loops form after phosphorus

implantation. In the simulations, a homogenous dislocation loop formation model [27] has been used to predict the distribution of dislocation loops in the end-of-range region.

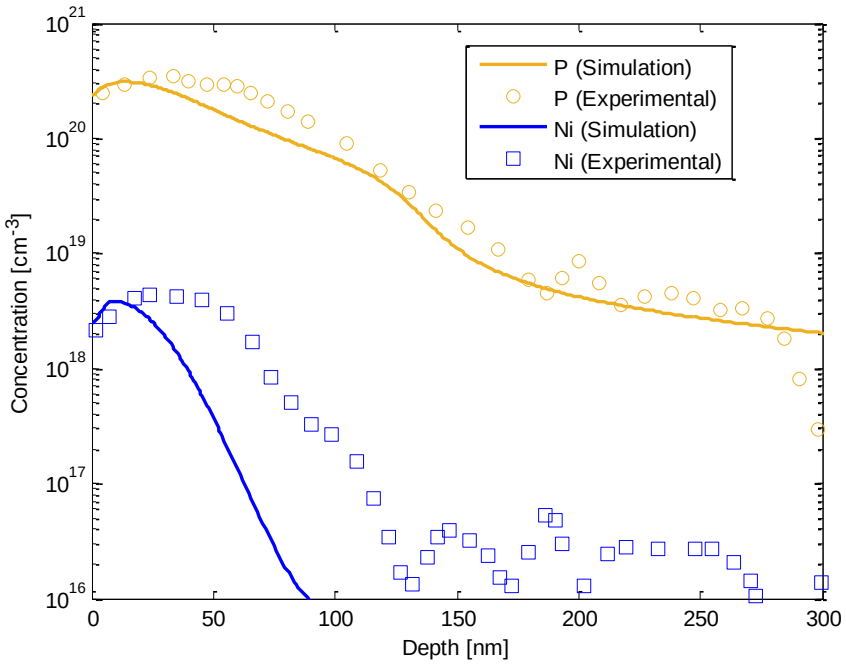

Figure 4.2. Simulated Ni and P profiles after annealing compared to SIMS data [31] (anneal of 5s at 1020℃ and 90min at 700℃).

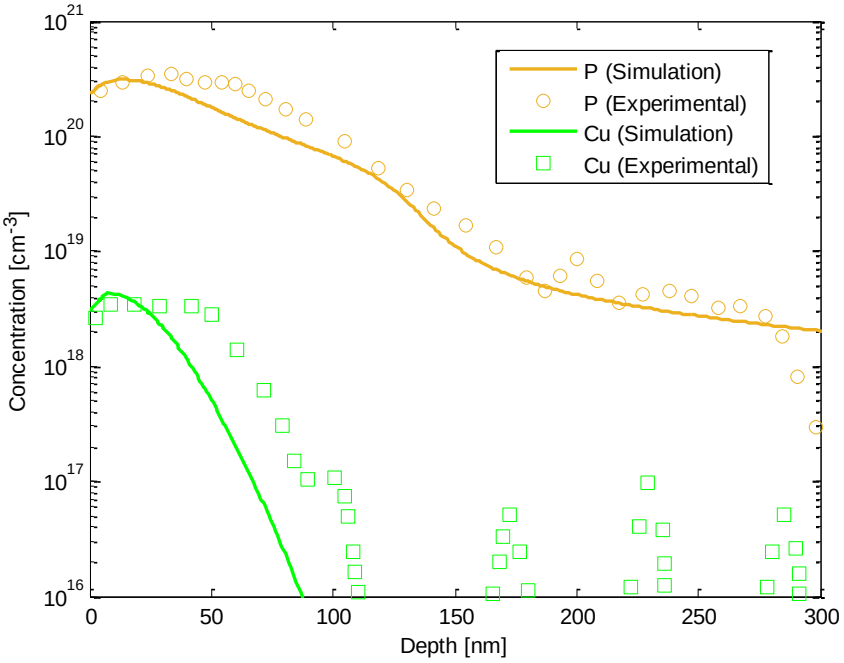

Figure 4.3. Simulated Cu and P profiles after annealing compared to SIMS data [31] (anneal of 5s at 1020℃ and 90min at 700℃).efficiency vs. bulk lifetime (The values are relative numbers).

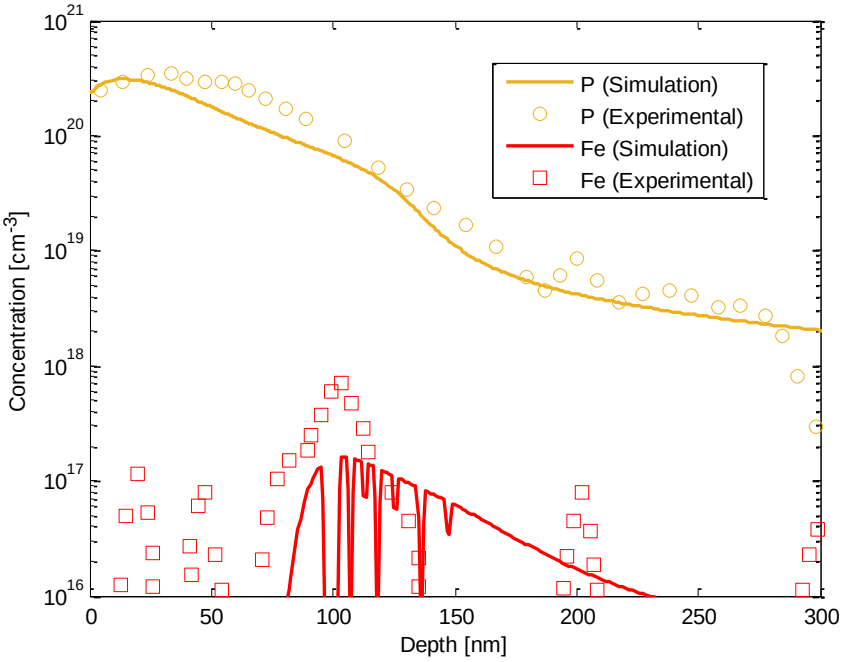

Figure 4.4. Simulated Fe and P profiles after annealing compared to SIMS data [21] (anneal of 5s at 1020℃ and 90min at 700℃).

4.2 COUPLING OF PROCESS AND DEVICE SIMULATIONS

The defect distribution can be translated into carrier lifetime throughout the wafer via the use of SRH recombination model in the device simulations. Thus, process and device simulations can effectively be coupled and the impact of a variety of processing conditions on the performance of lifetime sensitive devices can be assessed and optimized. In this work, process and device simulations are done within Sentaurus Device Platform [2] on a generic photodiode of a CMOS image sensor [33] to simulate the impact of different annealing conditions with different cool-down rates on wafer impurity redistribution and the resulting dark current of the photodiode.

4.2.1 *Photodiode Structure and Processing Conditions*

Beginning with a P-N junction formed at the front surface of an n-type, 600 μm-thick bifacial passivated silicon wafer, the back side of the wafer is implanted with phosphorus at 50 keV and with dose of 5×10^{15} atoms/cm^2 to introduce dislocation loops and P_4V clusters as proximity gettering sites for impurities around active device region. In addition, it is assumed that the surface of the screen oxide is contaminated with Fe, Cu, Mo, and W with equal doses. It is observed that, depending on the screen oxide thickness, the rate of penetration of surface metals into the silicon through the oxide by ion implantation is, at lowest, 0.1% for W, and maximum 10% for Fe [34]. Thus, the initial concentration of Fe, Cu, and Mo throughout the silicon wafer is defined by uniform concentration at 10^{13} cm^{-3} while W is defined at 10^{12} cm^{-3} before annealing. Finally the wafer is annealed at 1020℃ for 5s and cooled down from 1020℃ to 800℃ in 10s, and then to the room temperature with cool-down times of either 10s or 10min. Fig. 4.5 shows the P-N junction, and Fe redistribution and segregation to boron and dislocation loops formed by oxygen precipitation after annealing with 10s cool-down from 800℃ to room temperature.

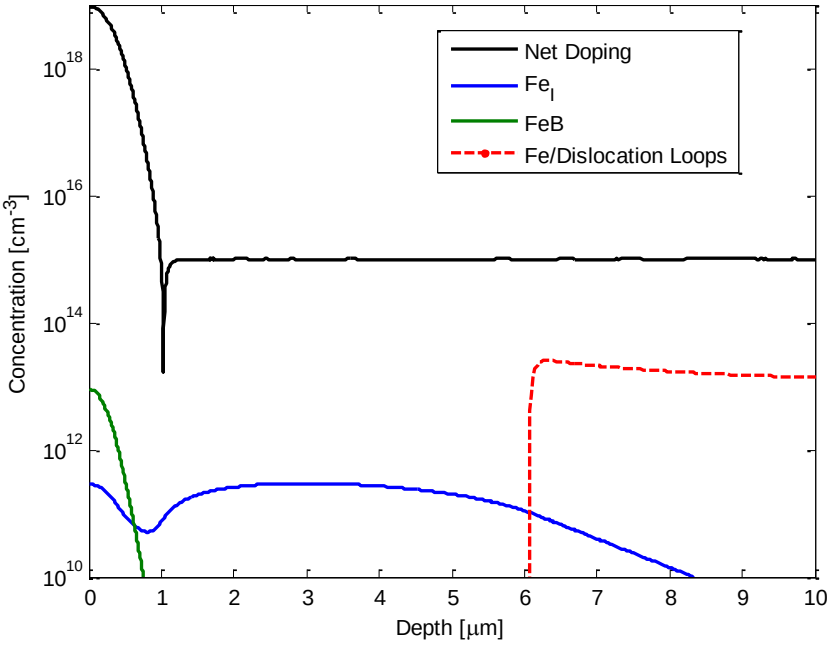

Figure 4.5. Doping concentration and simulated interstitial Fe, FeB pairs, and Iron-dislocation loops pairs formed from oxygen precipitation (cool-down rate of 10s from 800℃ to room temperature).

4.2.2 *Device Simulation Models*

The carrier recombination throughout the bulk at transition metals is modeled by a multi-trap SRH recombination model:

$$U = (np - {n_i}^2) \sum_j \left(A_j\right)^{-1} \tag{4.11}$$

$$A_j = \frac{n+n_i\, exp\left(\frac{E_j - E_i}{kT}\right)}{v_{thp} N_j \sigma_{pj}} + \frac{p+n_i\, exp\left(\frac{E_i - E_j}{kT}\right)}{v_{thn} N_j \sigma_{nj}} \tag{4.12}$$

In which, n and p are electron and hole concentrations, n_i is the intrinsic carrier concentration, E_j is the energy level of trap j within the silicon bandgap, E_i is the intrinsic fermi level, $v_{thn}$and v_{thp} are thermal velocities of electrons and holes respectively, σ_{nj} and σ_{pj} are electron and hole

capture cross sections of trap j respectively, and N_j is the density of active trap j which is calculated in the process simulations. The capture cross sections and trap energy levels are based on the literature and are shown in Table 4.4.

Table 4.4. Capture Cross Sections and Energy Levels of Defects in Silicon.

Metal	Defect Type	Location [eV]	σ_n [cm^{-2}]	σ_p [cm^{-2}]	Ref.
Cu	Donor	E_C-0.16	3.3×10^{-17}	$< 10^{-14}$	[38]
Fe	Donor	E_V+0.39	5×10^{-14}	7×10^{-17}	[35]
Mo	Donor	E_V+0.28	1.6×10^{-14}	6×10^{-16}	[35]
W	Donor	E_V+0.4	1.7×10^{-14}	6.6×10^{-16}	[36,37]

Total recombination or generation rate is dominated by Fe, Mo, and W having energies near the middle of bandgap and is less pronounced for Cu possessing a shallow donor level. Ni dominantly occupies a tetrahedral interstitial site in the silicon lattice and is electronically inactive. It becomes active when it pairs with vacancies and sits in a substitutional site in the lattice [39], however, since the concentration of Ni-vacancy pairs are negligible compared to other generation-recombination centers, it has a minor impact on the device performance. $NiSi_2$ precipitates are reported to dominate Ni related carrier recombination [40], however, modeling of Ni silicidation is not in the scope of this dissertation and is left for future works. As a result, Ni is excluded from the photodiode coupled process and device simulations and its impact on the carrier recombination is neglected.

Auger recombination is also taken into account using standard values for silicon [5]. The carrier mobility is modeled as by Masetti [4] with the DelAlamo band gap narrowing model [4] taken into account.

By incorporating the mentioned models and by solving the Poisson's equation and electron- and hole- continuity equations in the device simulations, the electrical characteristics of the device performance can be calculated.

4.2.3 *Analysis of the Results*

Fig. 4.6-4.9 demonstrate the impact of cool-down rates on metal distributions near the P-N junction. As the system cools, the dopants become immobile however metals continue to diffuse and segregate to boron rich base at the front side of the wafer and to the dislocation loops formed by oxygen precipitation throughout the wafer. P_4V clusters and dislocation loops formed from {311} clusters introduced by phosphorus implantation at the bottom of the wafer provide additional gettering sites for metal impurities with similar gettering behavior shown in Fig. 4.2-4.4. A slower cool-down rate allows for more segregation and reduces the density of interstitial metals which are active generation-recombination centers near the junction depth. Cu has the fastest diffusivity and as a result has the most segregation to the surface where is heavily doped with boron or phosphorus, whereas Fe is dominantly attracted towards the dislocation loops.

Simulations also identify that extended defects and P_4V clusters do not play an effective role in trapping W and Mo because of those metals' slow diffusivities. Similar gettering behavior from W and Mo is observed in the experiments [41] in which Carbon implantation with high doses was suggested as a more effective proximity gettering strategy. Carbon implantation at high doses results in carbon precipitation into SiC precipitates to which Mo and W have large binding energies of -3.22 eV and -3.36 eV respectively [42], while to proximity of the gettering sites to junction compensates for their slow diffusivities in Eq. (4.8).

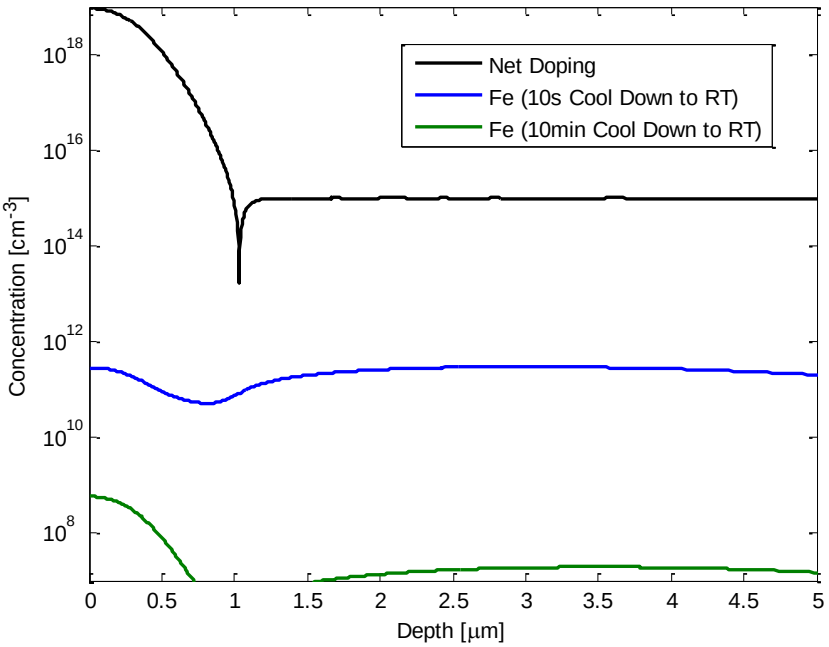

Figure 4.6. Close-up of the simulated interstitial Fe distribution near the P-N junction after 10s and 10min cool-downs from 800℃ to room temperature.

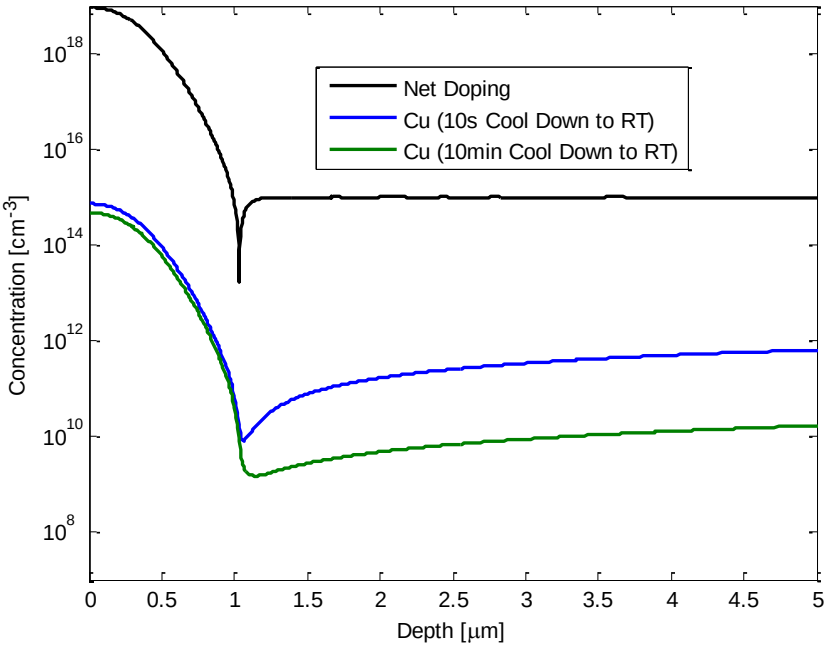

Figure 4.7. Close-up of the simulated interstitial Cu distribution near the P-N junction after 10s and 10min cool-downs from 800℃ to room temperature.

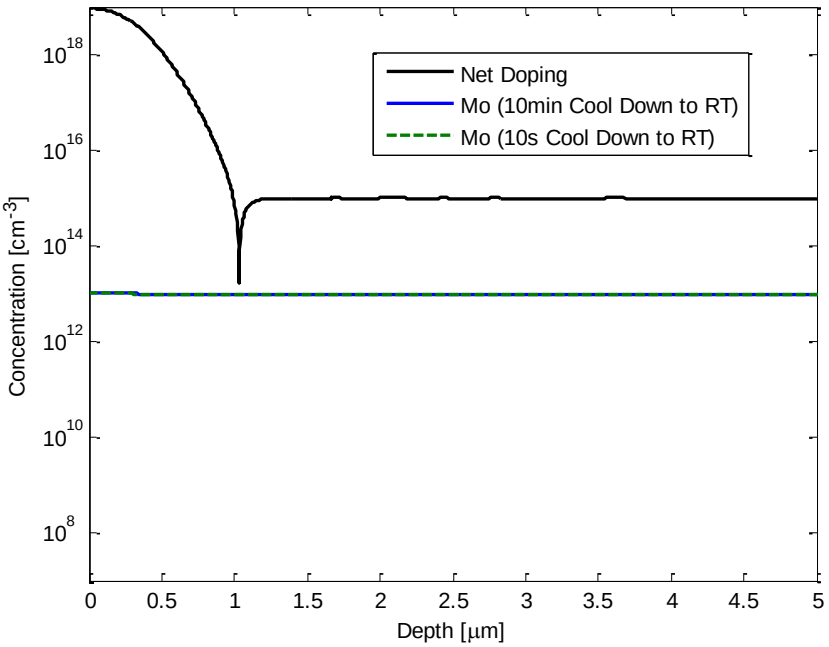

Figure 4.8. Close-up of the simulated interstitial Mo distribution near the P-N junction after 10s and 10min cool-downs from 800℃ to room temperature.

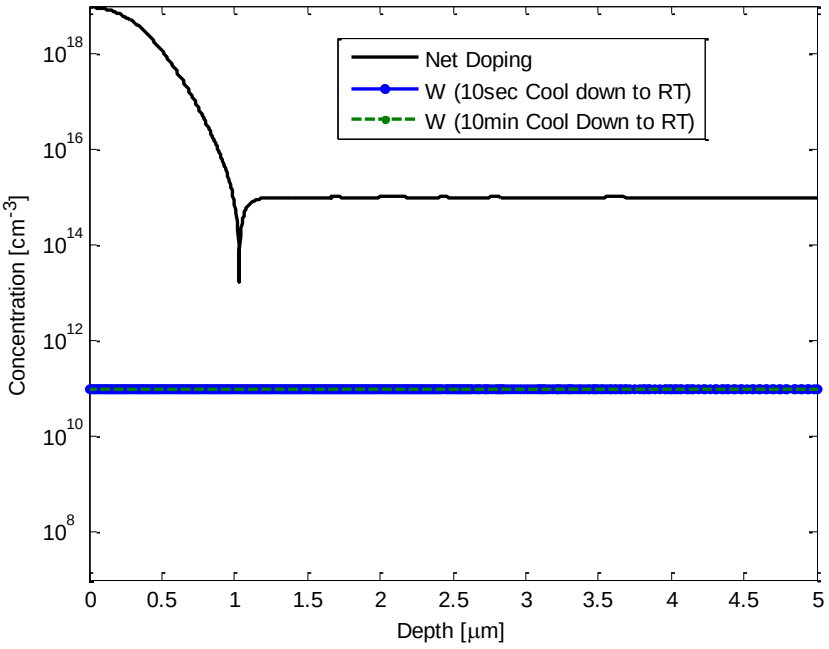

Figure 4.9. Close-up of the simulated interstitial W distribution near the P-N junction after 10s and 10min cool-downs from 800℃ to room temperature.

Fig. 4.10 shows the calculated total generation in the depletion region of the photodiode at the reverse bias of -5V with two different cool-down rates. The total generation is maximum in the depletion region and as a result the leakage current of the photodiode is dominated by the generation at this region. Fig. 4.11 shows the calculated leakage current of the device after annealing with two cool-down rates. As can be seen, slower cool-down rate has made a stronger reduction in the density of active impurities near the metallurgical junction; thus, the total generation and leakage current are decreased. The reduction in the leakage current for the 10min cool-down time is 48% relative to 10s cool-down time leading to better image sensing quality with larger dynamic range and less noise [33]. Longer cool-down times will not make a more significant improvement in the device performance due to the presence of Mo and W reluctant to be trapped by the gettering sites in the system and redistribute away from the depletion region of the diode.

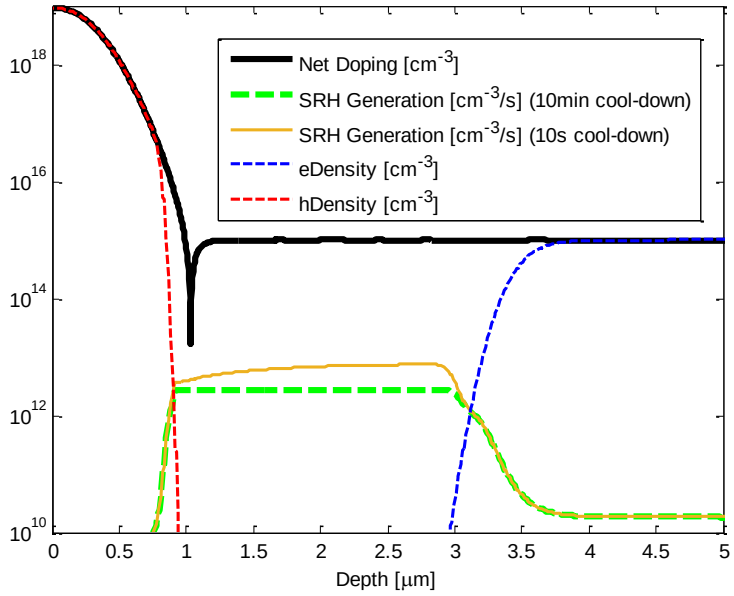

Figure 4.10. Close-up of the simulated SRH generation from defects in the depletion region of the photodiode, reversely biased at -5V, after 10s and 10min cool-downs from 800℃ to room temperature.

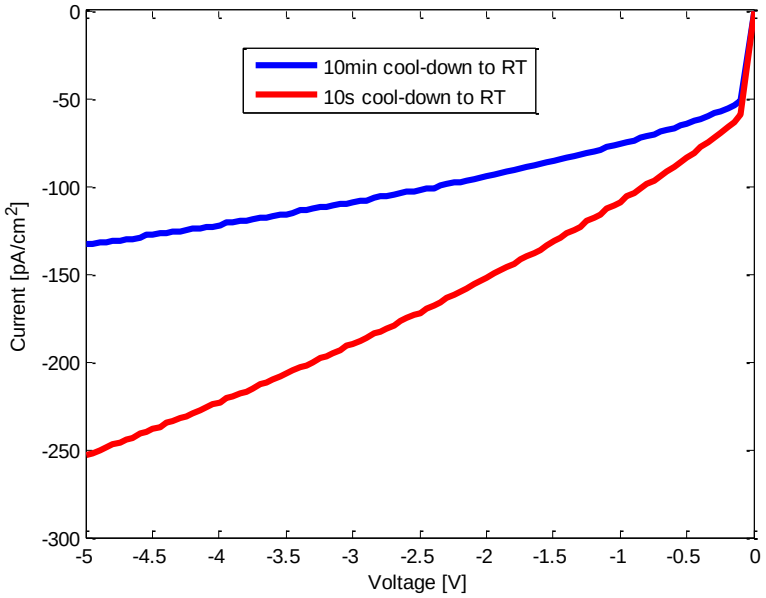

Figure 4.11. Simulated dark current of the photodiode after 10s and 10min cool-downs from 800℃ to room temperature.

4.3 SUMMARY

Continuum models for the gettering of transition metals (Fe, Ni, Cu, Mo, and W) were developed based on *ab initio* calculations and compared to available experimental data. The continuum models provide insight into the atomic processes and the kinetics governing the gettering and redistribution of the metals, thereby explaining the experimentally observed competitive gettering behavior of metals. In addition, process simulations were coupled with device simulations through SRH recombination model allowing one to calculate carrier lifetime and the resulting final performance of the photodiode of CMOS image sensors. We demonstrate how changes in the cool-down rate of annealing can help improve metal gettering without impacting doping profiles, and as a result, improve device performance. The result of this work is a comprehensive TCAD framework providing engineers with a tool process optimization and a cost effective way to assess

the impact of various processing conditions on device performance. The TCAD framework can easily be extended to other lifetime sensitive devices.

Chapter 5. CONCLUSIONS AND RECOMENDATIONS

The objective of this dissertation was to develop an accurate and reliable TCAD framework enabling us to predict the lifetime sensitive devices' performance based on their geometrical features and fabrication processes. The modeling was divided into three sub-tasks and for each sub-task the required calibrations were performed. In addition, it was shown how multiple process and device models can be run simultaneously providing stronger prediction over possible process and architectural variations.

In the process simulations, an accurate and versatile gettering process model was developed and based on that the experimentally observed gettering behavior of 5 transition metals was explained. The models successfully replicated the experimental data. The process modeling framework also demonstrated the complex atomic interactions between dopants, defects and metals. In addition, the process simulations were coupled with device simulations to predict the impact of the processing conditions and impurity distribution on the dark current of a photodiode. Although the framework was applied to a particular example, it is extensible to other devices, as well.

In the optical simulation, an accurate methodology for simulating textured surfaces was developed. This was critical, as most of the commercial solar cells apply surface texturing for better efficiencies. Lastly, the optical simulations were coupled with the device simulations to optimize the efficiency of a MWT solar cell. The framework was calibrated against the experimental measurements and the result was an excellent match to the measurements done on the fabricated sample solar cells. That provided us with a robust tool to optimize feasible geometrical variations on the device performance in a cost-effective way.

Although models were able to successfully replicate the experimental data, there is much room for improvement and further research:

- **Improving the dislocation loop model.** The model used in the process simulation predicted a homogeneous rate of dislocation loop formation from {311} clusters formed after ion implantations. However, the model was incapable of predicting the situations involving crystal amorphization after heavy ion implantations. In such situations the amorphous region starts to grow back to prefect crystalline from by solid phase epitaxial growth and the dislocation loops mostly form at right below the original crystalline/amorphous interface. Thus, a heterogeneous formation model must be developed and replaced. This will help the gettering models to have better prediction of the gettering of metals that are more attracted to dislocation loops such as Fe.
- **Development of Carbon/Interstitial clustering model.** As explained by the models, W and Mo are efficiency gettered by SiC precipitates. These precipitate form after heavy carbon implantation [41,42]. As a result modeling the clustering mechanism could be beneficial to improving the metal gettering model.

The primary novel result of this work was developing the gettering process model and optical simulation of textured solar cells and coupling the results with device simulations. With the future improvements, the TCAD framework has a great potential in simulating a wider range of process conditions for the ULSI devices, and helping the yield of silicon ICs and solar cells.

BIBLIOGRAPHY

[1] S. Alberth, "Forecasting Technology Costs via the Experience Curve -- Myth or magic?" Technological Forecasting and Social Change, Volume 75, Issue 7, September 2008.

[2] Sentaurus Device User Guide (Version D2010.03, March 2010).

[3] American Society for Testing and Materials (ASTM) Terrestrial Reference Spectra for Photovoltaic Performance Evaluation.

[4] P.P Altermatt, J. O. Schumacher, A. Cuevas, M. J. Kerr, S. W. Glunz, R. R. King, G. Heiser, A. Schenk, "Numerical modeling of highly doped Si:P emitters based on Fermi-Dirac statistics and self-consistent material parameters" *Journal of Applied Physics*, Volume 92, Number 6, 2002.

[5] R. S. Muller, T. I. Kamins, "Device Electronics for Integrated Circuits 3rd ed." John Wiley & Sons, 2003.

[6] D. K. Schroder, "Carrier lifetimes in Silicon" *IEEE Transactions on Electronic Devices*, VOL. 44, NO. 1, January 1997.

[7] W. Shochley, and W. T. Read. Phys. Rev. **87**, 835 (1952).

[8] H. Nagel, C. Berge, and A. G. Aberle, "Generalized analysis of quasi-steady-state and quasi-transient measurements of carrier lifetime in semiconductors" *J. Appl. Phys*. **86,** 6218 (1999).

[9] M. Bail, and R. Brendel, "Seperation of bulk and surface recombination by steady state photo conductance measurements" 16th European Photovoltaic Solar Energy Conference, I-5 May 2000, Glasgow.

[10] A. Cuevas, and R. A. Sinton, "Prediction of the open-circuit voltage of solar cells from the steady-state photoconductance" *Progress in Photovoltaics: Research and Applications*, VOL. 5, 79-90 (1997).

[11] R. A. Sinton, "Quasi-Steady-State photoconductance, a new method for solar cell material and device characterization" *IEEE* (1996).

[12] R. R. King, R. A. Sinton, and R. M. Swanson, "Studies of diffused phosphorus emitters: saturation current, surface recombination velocity, and quantum efficiency" *IEEE Transaction on Electronic Devices*, VOL. 37, NO. 2, February 1990.

[13] S. Gatz, T. Dullweber, and R. Brendel, "Evaluation of series resistance losses in screen-printed solar cells with local rear contacts" *IEEE Journal of Photovoltaics*, VOL. 1, NO. 1, July 2011.

[14] J. D. Plummer, M. D. Deal, P. B. Griffin, "Silicon VLSI Technology: Fundamentals, Practice, and Modeling" Prentice Hall, 2000.

[15] J. Hofstetter, D. P. Fenning, M. I. Bertoni, J. F. Lelievre, C. D. Canizo, T. Buonassisi, "Impurity-to-efficiency Simulator: Predictive Simulation of Silicon Solar Cell Performance Based on Iron Content and Distribution" *Progress in Photovoltaics: Research and Applications*, **19**:487-497 (2011).

[16] W. Schroter, R. Kuhnapfel, "Model Describing Phosphorus Diffusion Gettering of Transition Elements in Silicon" *Applied Physics* Letters **56**, 2207, 1990.

[17] P. S. Plekhanov, R. Gafiteanu, U. M. Gosele, T. Y. Tan, "Modeling of Gettering of Precipitated Impurities from Si for Carrier Lifetime Improvement in Solar Cell Applications" *Journal of Applied Physics* **86**, 2453, 1999.

[18] S. M. Myers, M. Seibt, W. Schroter, "Mechanisms of Transition-Metal Gettering in Silicon" *Journal of Applied Physics* **88**, 3795, 2000.

[19] A. A. Istratov, W. Huber, E. R. Weber, "Modeling of Competitive Gettering of Iron in Silicon Integrated Circuit Technology" *J. Electrochem. Soc.*, VOL. 150, Issue 4, 2003.

[20] A. L. Smith, K. Wada, L. C. Kimerling, "Modeling of Transition Metal Redistribution to Enable Wafer Design for Getterinh" *J. Electrochem. Soc.*, VOL. 147, Issue 3, 2000.

[21] W. Kresse, and J. Hafner. Phys. Rev. B **47**, 558 (1993).

[22] W. Kresse, and J. Furthmuller. Phys. Rev. B **54**, 11169 (1996).

[23] Sentaurus Process User Guide (Version J-2014.09, September 2014).

[24] P. Pichler, "Intrinsic Point Defects, Impurities, and Their Diffusion in Silicon" Springer, 2004.

[25] S. T. Dunham, "A Quantitative Model for the Coupled Diffusion of Phosphorus and Point Defects in Silicon" *J. Electrochem. Soc.*, Volume 139, Number 9, September 1992.

[26] R. Chen, B. Trzynadlowski, S. T. Dunham, "Phosphorus Vacancy Cluster Model for Phosphorus Diffusion Gettering of Metals in Si" *Journal of Applied Physics* **115**, 054906, 2014.

[27] A. H. Gencer, S. T. Dunham, "A Combined Model for {311} Defect and Dislocation Loop Evolution: Analytical Formulation of Kinetic Precipitation Model" *Journal of Applied Physics* **91**, 2883, 2002.

[28] B. Trzynadlowski, S. T. Dunham, "A Reduced Moment-Based Model for Oxygen Precipitation in Silicon" *Journal of Applied Physics* **114**, 243508, 2013.

[29] Y. Oh, D. E. Ward, "A Calibrated Model for Trapping of Implanted Dopants at Material Interface During Thermal Annealing" *IEEE* (1998).

[30] R. D. Chang, J. R. Tsai, "Loss of Phosphorus due to Segregation at Si/SiO2 Interfaces: Experiments and Modeling" *Journal of Applied Physics* **103**, 053517, 2008.

[31] K. Saga, "Gettering Behavior of Transition Metals in Low Energy, High Dose Ion Implanted Silicon" *Solid State Phenomena*, VOL. 187, 2012.

[32] G. Hobler, E. Langer, S. Selberherr, "Two-Dimensional Modeling of Ion Implantation with Spatial Moment" *Solid-State Electronics*, VOL. 30, No. 4, 1987.

[33] A. Gamal, H. Eltoukhy, "CMOS Image Sensors: An Introduction to the Technology, and Performance Limits, Presenting Recent Developments and Future Directions" *IEEE* Circuits & Devices Magazine (2005).

[34] K. Saga, R. Ohno, D. Shibata, S. Kobayashi, K. Sueoka, "Behavior of Transition Metals Penetrating Silicon Substrate Through SiO2 and Si3N4 Films by Arsenic Ion Implantation and Annealing" ECS Journal of *Solid State Science and Technology*, **4** (5) pp.131-136, 2015.

[35] D. Macdonald, L. J. Geerligs, "Recombination Activity of Interstitial Iron and Other Transition Metal Point Defects in P- and N-Type Crystalline Silicon" Applied Physics Letters, VOL. 85, NO. 18, 2004.

[36] S. Boughaba, D. Mathiot, "Deep Level Transient Spectroscopy Characterization of Tungsten-Related Deep Levels in Silicon" *Journal of Applied Physics* **69**, 278, 1991.

[37] T. Ando, S. Isomae, C. Munakata, T. Abe, "Deep-Level Transient Spectroscopy on P-Type Silicon Crystals Containing Tungsten Impurities" *Journal of Applied Physics* **70**, 5401, 1991.

[38] W. B. Henley, D. A. Ramappa, L. Jastrezbski, "Detection of Copper Contamination in Silicon by Surface Photovoltage Diffusion Length Measurements" *Applied Physics Letters* **74**, 278, 1999.

[39] H. Indusekhar, V. Kumar, "Electrical Properties of Ni-Related Deep Levels in Silicon" *Journal of Applied Physics* **61**, 1449, 1987.

[40] A. A. Istratov, E. R. Weber, "Electrical Properties and Recombination Activity of Copper, Nickel and Cobalt in Silicon" *Applied Physics A*, VOL. 66, Issue 2, 1998.

[41] F. Russo, G. Moccia, G. Nardone, R. Alfonsetti, G. Polsinelli, A. D'Angelo, A. Patacchiola, M. Liverani, P. Pianezza, T. Lippa, M. Carlini, M. L. Polignano, I. Mica, E. Cazzini, M. Ceresoli, D. Codegoni, "Proximity Gettering of Slow Diffuser Contaminations in CMOS Image Sensors" *Solid-State Electronics* **91**, 2014.

[42] Y. Jin, S. T. Dunham, "Modeling of Carbon Clustering and Associated Metal Gettering" ECS Transactions, VOL. 64, 2014.

[43] A. Kitai, "Principles of Solar Cells, LEDs, and Diodes-The Role of the PN Junction" Hoboken: Wiley, 2011.

[44] www.globalwarmingart.com.

[45] K. Bothe, R. Sinton, J. Schmidt, "Fundamental Born-Oxygen-related Carrier Lifetime Limit in Mono and Multicrystalline Silicon" Prog. Photovolt: Res. Appl. 2005; 13:287-296.

[46] B. E. Deal, M. Sklar, A. S. Grove, E. H. Snow, "Characteristics of the Surface-State Charge (Qss) of Thermally Oxidized Silicon" J. Electrochem. Soc.: SOLID STATE SCIENCE, 1967.

[47] E. D. Palik, "Handbook of Optical Constants of Solids" Academic Press NY, 1985.

[48] A. Mesli, T. Heiser, E. Mulheim, "Copper Diffusivity in Silicon: A re-examination" Material Science and Engineering: B, VOL. 25, 141-146 (1994).

[49] S. V. Koveshnikov, G. A. Rozgonyi, “Iron Diffusivity in Silicon: Impact of Charge State” *Applied Physics Letters*, VOL. 66, 1995.

[50] T. Abe, “Proceedings of the Third International Symposium on Defects in Silicon” Electrochemical Society, 1999.

[51] A. Y. Kuznetsov, B. G. Svensson, “Nickel Atomic Diffusion in Amorphous Silicon” *Applied Physics Letters*, VOL. 66, 1995.

[52] A. D. Luca, A. Portavoce, M. Texier, C. Grosjean, N. Burle, V. Oison, B. Pichaud, “Tungsten Diffusion in Silicon” *Journal of Applied Physics* **115**, 013501, 2014.

[53] P. Fastenko, S. T. Dunham, G. Henkelman, “Modeling of annealing of high concentration arsenic profiles” Mat. Res. Soc. Symp. Proc. Vol. 669, 2001.

APPENDIX A
MASETTI CARRIERS' MOBILITY MODEL

Quantum-Mechanical calculations indicates that lattice atoms' vibrations at temperatures $T > 0K$, disturb the periodicity of the lattice and thus allow energies (phonons) to be transferred between carriers and the lattice. Interaction between carriers and phonons scatter the carriers. In addition, impurities (dopants) and crystal defects (or grain boundaries in polycrystalline materials) also disturb the periodicity of the lattice and thus scatter free carriers and reduce their mobility. As a result, mobility of carriers is affected by multiple scattering processes and the effective mobility of carriers is found by combining the mobility due to each scattering process:

$$\frac{1}{\mu} = \sum_i \frac{1}{\mu_i} \tag{A.1}$$

The doping dependent effective mobility of electrons and holes in crystalline silicon has been measured and empirically modeled by Masetti's Mobility Equation [2]:

$$\mu_{doping} = \mu_{min1} \exp\left(\frac{P_C}{N_{A,0}+N_{D,0}}\right) + \frac{\mu_{const}-\mu_{min2}}{1+((N_{A,0}+N_{D,0})/C_r)^{\alpha}} - \frac{\mu_1}{1+(C_S/(N_{A,0}+N_{D,0}))^{\beta}} \tag{A.2}$$

where $N_{A,0}$and $N_{D,0}$ are acceptor and donor concentrations respectively, and the rest of the parameters' values are listed in Table A.1. In addition, Fig. A.1 shows the mobility of carriers with respect to total doping concentration based on Eq. (A.2).

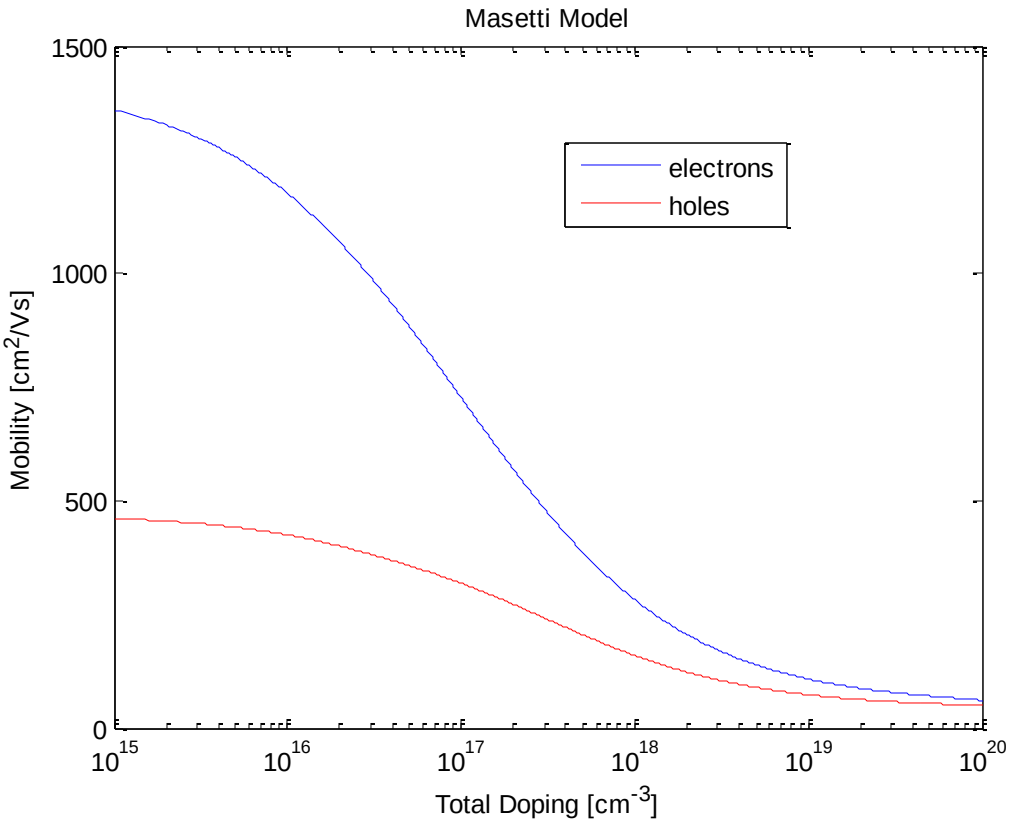

Figure A.1. Mobility of carriers modeled by Eq. (A.2).

Table A.1. Masetti model parameters. Reproduced from Ref. [2].

Parameter	Electrons	Holes	Unit
μ_{min1}	52.2	44.9	cm^2/Vs
μ_{min2}	52.2	0	cm^2/Vs
μ_1	43.4	29	cm^2/Vs
P_C	0	9.23×10^{16}	cm^{-3}
C_r	9.68×10^{16}	2.23×10^{17}	cm^{-3}
C_s	3.42×10^{20}	6.1×10^{20}	cm^{-3}
α	0.68	0.719	1
β	2	2	1

APPENDIX B
PAIRING REACTION EQUILIBRIUM CONSTANT

From mass action, if the binding reactions (Eq. (4.5)–(4.7)) are near equilibrium, with dilute solution approximation ($C_A \ll C_{Si}$), the concentration of pairs is:

$$A + B \Leftrightarrow A/B \tag{B.1}$$

$$C_{AB} = \frac{\theta_{AB}}{\theta_A \theta_B} \frac{C_A C_B}{C_{Si}} \exp\left(\frac{-(\Delta H_f - T\Delta S_f)}{kT}\right) \tag{B.2}$$

where, C_A is the concentration of metals (e.g. Cu, Fe, Ni, Mo, and W), C_B is the concentration of the gettering sites (e.g. boron, P4V, and dislocation loops), C_{Si} is the silicon atomic density, θ is the configuration entropy of reactants and pairs, $\Delta H_f = -E_{Binding}$ is the enthalpy of formation of the pairing reactions which is calculated by *ab initio* DFT calculations (Table 4.1), and ΔS_f is the entropy of formation of the pairing reactions. The entropy terms can be lumped in γ and Eq. (B.2) can be rewritten as:

$$C_{AB} = \frac{C_A C_B}{\gamma C_{Si} \exp\left(\frac{\Delta H_f}{kT}\right)} \tag{B.3}$$

$$\gamma = \exp\left(\frac{-\Delta S}{k}\right) \tag{B.4}$$

Table B.1 lists the values of γ optimized to achieve minimum difference between simulated and SIMS profiles of Cu/P_4V, Fe/ P_4V, and Ni/ P_4V pairs. The entropy change is on the order of 10k and as a result all the calibrated values are within a reasonable range.

Table B.1. Calibrated γ used in the pairing reactions.

Reaction	γ	ΔS
Cu/P_4V	4.32×10^{-3}	5.44k
Ni/ P_4V	0.72×10^{-3}	7.23k
Fe/ P_4V	4.32	-1.46k